Improved modeling of neutron-induced reactions on chlorine isotopes aided through new (n, p) and (n, α) measurements at LANSCE

K. Hanselman,* S. A. Kuvin,† H. Y. Lee, T. Kawano, S. Essenmacher, P. Gastis, H. Jayatissa, and S. N. Paneru
Los Alamos National Laboratory, Los Alamos, New Mexico 87545, USA

H. I. Kim
Nuclear Physics Application Research Division, Korea Atomic Energy Research Institute, Yuseong-gu, Daejeon, Korea

A. T. Cisneros and M. Wargon
TerraPower LLC, Bellevue, Washington 98008, USA

(Received 1 May 2024; accepted 9 July 2024; published 19 August 2024)

Renewed interest in neutron-induced reactions on chlorine isotopes has led to a surge of new measurements. Much of this effort has been spurred to inform on the many modern applications in which chlorine plays an important role, e.g., molten salt reactor design and reaction rate calculations for nuclear astrophysics. In this work, we report new ^{35}Cl(n, p) and ^{35}Cl(n, α) partial and total cross sections measured at the Los Alamos Neutron Science Center using the LENZ [Low-Energy (n, Z)] experimental setup, complementary to those published previously. The data span incident neutron energies from 300 keV to 12 MeV, extending beyond the previous study, and are consistent in magnitude and fluctuation. We also report on an effort at LANL to reanalyze the ^{35}Cl(n, X) system in the fast (statistical) energy range under a Hauser-Feshbach formalism, including the latest data. The leading results are an overall reduction in neutron absorption in the fast-energy range compared to base (global) optical model values, due to the low level density of the compound (^{36}Cl) system, but a net increase in cross section at the higher energies (>10 MeV) modeled through an enhanced preequilibrium component, an energy range potentially relevant for fusion applications. The cross-cutting impacts of these results on some of the referenced applications are discussed, including extensions of the analysis to neighboring isotopes. The calculations described here provide a foundation for a future update to the ENDF/B nuclear data library.

DOI: 10.1103/PhysRevC.110.024609

I. INTRODUCTION

The challenge of modeling reactions on nuclei near the $N = Z = 20$ shell gap is a familiar one. Nuclei here feature level densities typically too high for purely microscopic or R-matrix treatments, yet which are still prone to structure-based features and fluctuations that deviate from statistical Hauser-Feshbach predictions. For neutron-induced reactions on ^{35}Cl, due to a low level density near the neutron separation energy of ^{36}Cl, formation of a compound nucleus by an incident neutron is strongly suppressed, resulting in reduced neutron absorption at energies and channels relevant for certain applications [1]. In general, the optical potentials for lighter elements tend to deviate from a global behavior seen in the wider mass range, and the nuclear structure effects become more visible. In the ^{35}Cl case, the nonstatistical nature of the level density in ^{36}Cl may bring some unanticipated local energy dependence to the phenomenological optical potential.

Compounding these difficulties has been the lack of adequate experimental data for ^{35}Cl to constrain the reaction modeling, especially for incident neutron energies above 100 keV. The (n, p) and (n, γ) reactions on the stable ($A = 35$ and $A = 37$) and long-lived radioactive ($A = 36$) isotopes of chlorine were previously studied from thermal neutron energies up to a few 100 keV, primarily to constrain stellar and explosive nucleosynthesis reaction network calculations [2–5]. These measurements, combined with studies of the $(n,$ total) cross section through neutron transmission measurements, also provided very important constraints to criticality calculations of the thermalized neutron spectra in traditional fission reactor designs [6]. Hence, the fidelity of evaluated nuclear data for chlorine, captured in evaluations such as ENDF/B [7] and JENDL [8], were of fairly high quality up to $E_n \simeq 100$ keV.

Above this energy, some measurements of ^{35,37}Cl(n, p), ^{35,37}Cl(n, α), and ^{35}Cl$(n, 2n)$ were studied at energies greater than 10 MeV, a range important for D-T fusion applications. In the intermediate region, between 100 keV and 10 MeV, aside from old measurements of ^{35}Cl(n, α) between 2–4 MeV [9,10] and limited differential neutron scattering data [11], the only available data were in the form of neutron transmission measurements on natural abundance targets (e.g., Refs. [12–15]). These transmission measurements determine the total neutron reaction cross section, which is typically

*Contact author: khanselman@lanl.gov
†Contact author: kuvin@lanl.gov

 ©2024 American Physical Society

dominated by the neutron scattering reaction and cannot discriminate the smaller neutron absorption cross sections. As a result, the neutron total cross sections were constrained by experimental data in the available nuclear data evaluations but critical reactions like (n, p) and (n, n') were not. For fast-spectrum advanced reactor designs that employ chloride salts as a coolant and/or fuel [16], the lack of experimental constraints on the (n, p) reaction in the existing evaluated nuclear data leads to differences in reactivity by 2% or more, leading to large uncertainties in calculations of criticality [17–19]. An urgent need for new measurements and reevaluation of chlorine nuclear data was requested by industry users in the Nuclear Energy Agency (NEA) high-priority request list and highlighted in multiple recent publications [17,19]. This has led to a major push in recent years to improve the community's knowledge on neutron-induced reactions on chlorine isotopes.

New experimental data on ^{35}Cl(n, p) were published in Refs. [1,20,21], on ^{35}Cl(n, α) in Refs. [1,22], and preliminary (n, p_0) cross section data derived from CLYC (Cs_2LiYCl_6:Ce) detector efficiencies were described by Warren [23]. All the measured (n, p) data demonstrated a systematic discrepancy with the current ENDF/B-VIII.0 library, being both lower in overall magnitude (in the statistical region) and prone to fluctuations in the cross section not captured consistently by the statistical average. Further, among the measurements the scale of the data of Ref. [1] was found to be inconsistent with that of Ref. [21] by about a factor of 2.5, further highlighting the critical need for new measurements. The fast reactor community typically requires uncertainties at the level of 5% or better on this reaction channel [19].

Over the past few years, multiple new measurements have been performed on ^{35}Cl across multiple reaction channels. Part of this work will be to report on the latest of these measurements performed at the Los Alamos Neutron Science Center (LANSCE). Additionally, with the improved data now available, a new statistical Hauser-Feshbach analysis of the ^{35}Cl(n, X) system has been undertaken to improve the knowledge of reactions in this mass range and to constrain the sensitivities relevant to the Molten Chloride Reactor Experiment (MCRE), for which collaborators at TerraPower (TP) are leading [24]. This analysis forms the foundation for a new evaluation of chlorine nuclear data, particularly for energy ranges and reaction channels where experimental data continue to be lacking. The remainder of the paper will be dedicated to that effort, including its modeling challenges, extensions to neighboring nuclei, and connections to other applications such as nuclear astrophysics libraries.

Section II presents the new measurements of ^{35}Cl(n, p) and ^{35}Cl(n, α) performed at LANSCE with improved sensitivity and precision over the previous study [1]. From there, Sec. III dives into the application of statistical Hauser-Feshbach theory to the global data on chlorine isotopes, including discussion on the difficulties in reaction theory modeling in this mass range. Section IV covers model uncertainty quantification and Sec. V the impact of the present results on select applications. A summary and conclusion follow respectively in Sec. VI.

II. MEASUREMENTS OF ^{35}Cl(n, p) and ^{35}Cl(n, α) at LANSCE

A. Experimental setup

Reference [1] provides a general discussion on measurements with fast neutrons at the Weapons Neutron Research (WNR) facility using the LENZ [Low-Energy (n, Z)] experimental setup. In this section, a summary of the most critical differences with that previous measurement is presented.

In this work, the measurements were performed over the 2022 and 2023 run cycles of the LANSCE accelerator, once again utilizing the 15R and 90L flight paths at WNR. These two flight paths represent two different angles and distances from the spallation neutron source and therefore two different neutron flux profiles. The 15R measurement (at a distance of 15.2 m) was optimized for higher incident neutron energies, while at 90L, at a distance of 8.2 m, neutrons could be resolved down to approximately 100 keV; however, due to the rapidly decreasing ^{35}Cl(n, p) cross section and strong contributions from the LANSCE proton dark current, we were limited to measure the cross sections down to just below 300 keV in this work.

For this study, isotopically enriched [99.35(2)%] samples of ^{35}Cl as silver chloride and sodium chloride were thermally evaporated onto 1.5 μm thick gold backings at the University of Notre Dame. Initial target characterization was performed using scanning electron microscopy (SEM), x-ray fluorescence (XRF), and energy dispersive spectroscopy (EDS) to evaluate the uniformity of the targets and identify potential impurities, which were found to be negligible. The targets were further characterized with α-energy loss measurements with radioactive mixed-isotope α sources and using in-beam tests of Rutherford backscattering (RBS) of α particles delivered using the Tandem Van de Graff accelerator at Ohio University. The thicknesses derived for the NaCl and AgCl targets were 393(14) μg/cm^2 and 631(22) μg/cm^2, respectively, consistent with the 380(38) and 600(60) initially estimated when monitoring the nominal thickness of the foils during evaporation using a 6 MHz AT-cut quartz thickness monitor. Here, the uncertainty on the thickness monitor is based on typical expectations, whereas the uncertainty from the RBS and α-source measurements is derived from deviations in energy loss due to target effects such as porosity and interference from the backing materials. Compared to the $\approx$5.9 μm brass backing of the previous study [1], the charged particle backgrounds are significantly suppressed due to the higher Z of the thinner gold. The AgCl target was used at 15R and the NaCl target at 90L.

Both flight paths also used different configurations of Micron S1-type annular double-sided silicon detectors. The measurements at 15R used a thin-thick ΔE-E telescopic setup for particle identification (PID) whereas 90L employed rise-time pulse shape analysis similar to that described in Ref. [25]. Reaction Q values were reconstructed kinematically from the detected energy and angle and, when combined with the PID methods, could be used to extract (n, p) and (n, α) partial and total integrated cross sections. The detectors were set up to cover different forward and backward angles (Table I) to limit the uncertainty associated with the angular distribution in the

TABLE I. Summary of experimental setups at WNR. Both samples were on 1.5 μm-thick gold backings. Detector positions are given relative to the sample, with positive distances downstream.

Flight Path	Sample	Density	Sample-Target Dist.
15R	AgCl	631(22) μg/cm^2	15.192(37) m
90L	NaCl	393(14) μg/cm^2	8.293(15) m
		S1 Detector Information	
Run Cycle	FP	Thickness	Nominal Lab. Angles
2022	15R	65 μm	27–46°
		1000 μm	22–39°
2022	90L	300 μm	41–60°
		300 μm	133–152°
2023	15R	65 μm	134–153°
		1000 μm	141–158°

determination of the overall detection efficiency. The two separate measurements at 15R, with detectors at either forward or backward angles, have been combined in an uncertainty-weighted average for the final results, prior to comparison with the 90L measurements.

The neutron flux was again monitored using fission standard (^{235}U and ^{238}U) foils in ionization chambers. The ^{235}U(n, f) and ^{238}U(n, f) cross sections provided the relative normalization for the extraction of the (n, Z) cross sections. Additionally, the overall neutron flux normalization and solid angle coverage of the detectors was validated by measuring neutron elastic scattering on hydrogen, a standard at these energies, using a CH_2 target. Summaries of the experimental setups are provided in Table I and associated uncertainties in Table II.

B. Data analysis

As in previous LENZ measurements, the outputs from the Mesytec MPR-16 preamplifiers are fed directly into 500 MS/s sampling CAEN 1730 digitizers. Partial waveforms from each silicon detector hit are digitized and recorded over a length of 1.6 μs for off-line optimization of energy and timing filters. Sealed radioactive α-decay sources are used to calibrate the pulse-height scale of each detector and to validate the geometric efficiency of the detectors, determined

TABLE II. Uncertainties associated with the current measurements of n + ^{35}Cl at LANSCE.

Source	Relative Uncertainty
Neutron flux	4–5%
Detection efficiency	2%
Number of ^{35}Cl target atoms	3.5%
Dead time	$\ll$ 1%
Angle integration[a]	2–8%
Additional backgrounds above 5 MeV[b]	2–7%
Statistical uncertainties/100 keV bin	typ. 1–2%

[a]2–4 % for (n, p) and 2–8 % for (n, α).
[b]Assuming a 20% uncertainty in the expected ^{23}Na yields.

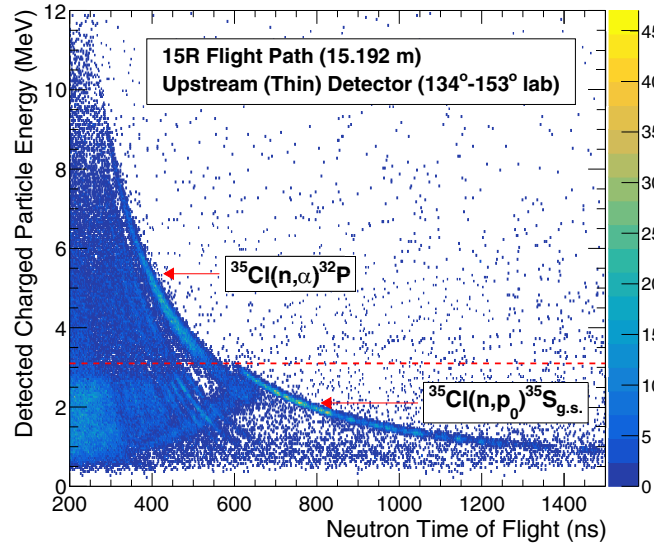

FIG. 1. Kinematic plot for the thin detector of the upstream ΔE-E telescope at 15R. The dashed red line denotes the kinetic energy at which protons from the target begin punching through the detector, serving as the primary form of PID.

using Monte Carlo simulations. The difference in detector response between incident protons and α particles is typically dominated by energy loss effects in the target and dead layers of the detector, which is tested using a 100 μg/cm^2 CH_2 target to measure hydrogen elastic scattering over a broad range of energies. ^{1}H(n, n) is considered a reference standard [26] so it is also used as an additional validation of the overall normalization involving the incident neutron flux and the efficiency of the silicon detectors. An example of measured charged particle energy versus neutron time-of-flight correlations for the thin (ΔE) detector at 15R is shown in Fig. 1. After characterizing backgrounds, these quantities, in addition to the angle of the detected charged particle, are then used to reconstruct the Q value of an assumed (n, Z) reaction in a specific neutron energy bin. Examples of these kinematically reconstructed Q-value spectra are shown in Fig. 2, for ^{35}Cl(n, p) ^{35}S and ^{35}Cl(n, α) ^{32}P specifically. These spectra are used to isolate the contributions from particular reaction channels and for identifying the sources of potential background reactions, as discussed in the following section. The partial yields are obtained from either integrating or fitting the individual channels, as needed, which are summed together with the integration over the remainder of the background-subtracted spectrum to be used in the determination of the total (n, p) and (n, α) cross sections.

Background considerations

With the replacement of the brass target backings with pure gold, the interference caused by reactions on copper and zinc in the previous measurement were eliminated. The primary source of background then became proton dark current from the LANSCE beam facility, described in Ref. [1], which was more pervasive for the data taken in the 2022 run cycle. The fractional contribution of these events throughout the

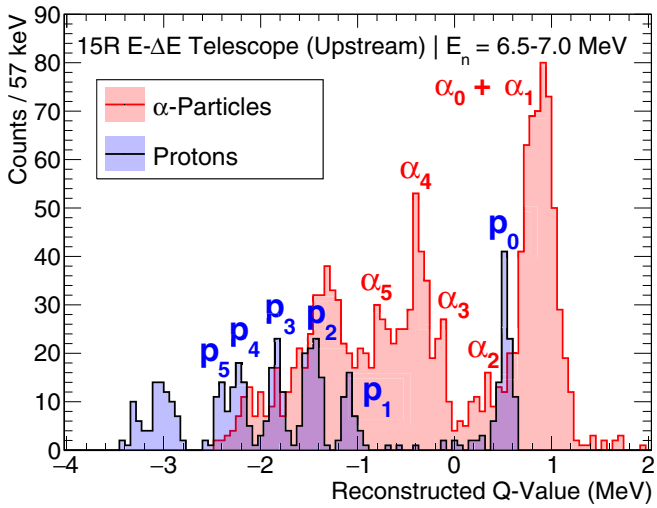

FIG. 2. Example spectra of Q-value reconstruction for the (upstream) ΔE-E telescope at 15R. A peak label of "p_x" indicates a proton from the ^{35}Cl(n, p_x) reaction, and similarly for (n, α_x). Particle separation is provided by the punch-through energy threshold of protons through the thin (65 μm) detector. Note also the significant lack of background compared to the previous study (e.g., Fig. 5 of Ref. [1]).

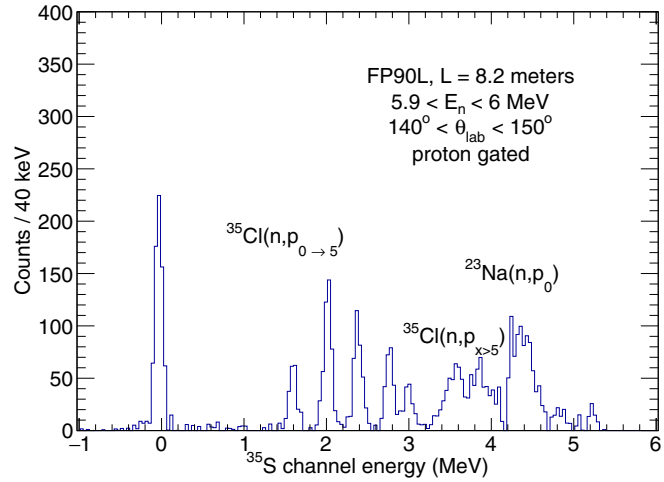

FIG. 3. Measured excitation spectrum at the 90L flight path. The relative contributions due to ^{23}Na(n, p) to the yield are consistent with expectations based on simulations using the ENDF/B-VIII.0 evaluation as an input.

experiment was monitored using a γ-sensitive facility monitor, consisting of plastic scintillators, at the 90R flight path, giving feedback to the operators for on-line proton beam optimization. In the LENZ data, the dark current contribution to the shape of this background is repeated over the entire frame and can be characterized and subtracted for each neutron energy bin. Alternatively, the contribution can be modeled using a polynomial background when fitting the peaks corresponding to the particular ^{35}Cl(n, X) reaction channels of interest.

Finally, background lines due to ^{28}Si$(n, p)^{28}$Al and ^{28}Si$(n, \alpha)^{25}$Mg are often observed at energies above $E_n = 5$ MeV. However, a majority of these events can be rejected through the particle identification and rise-time veto gates that are used to reduce background contributions from charged particle sources that do not originate from the target position. The remaining contributions are characterized through measurements with the gold backing alone (without sample deposits).

With the dark current and neutron induced backgrounds characterized, the remaining yields from (n, Z) reactions on NaCl and AgCl can be used to determine the (n, p) and (n, α) cross sections on ^{35}Cl. For the NaCl targets, (n, p) and (n, α) reactions on ^{23}Na become non-negligible above 5 MeV in incident neutron energy so a background subtraction is applied based on yields expected from the ENDF/B-VIII.0 evaluation. A 20% uncertainty is adopted for the scale of the ^{23}Na induced yields and results in a 2–7 % relative uncertainty in the background subtracted yields, as given in Table II. The contribution due to ^{23}Na(n, p) is labeled in Fig. 3, clearly visible on top of the continuum of states from ^{35}S. For 15R, charged particle backgrounds due to reactions on silver in the AgCl target are much more suppressed, requiring no additional correction for the data presented here.

C. Results

Due to key differences between the measurements at 15R and 90L (described in the previous section), we present the cross section results from each separately; however, the two 15R data sets (upstream and downstream) have been averaged together (weighted by their uncertainties) to minimize uncertainties from statistics and the angular distribution efficiency corrections. The new (n, p_0) and (n, p) total cross sections are shown in Fig. 4, relevant partial (n, p_x) in Fig. 5, and all measured (n, α) channels in Fig. 6, all against relevant data from the literature. Tables of the experimental total cross sections are provided in the Appendixes.

1. Data comparison: ^{35}Cl$(n, p)^{35}$S

The latest (n, p) results are consistent with the previous study over the energy range 600 keV to 6 MeV. By extending down to 300 keV, the data also resolve multiple new resonancelike structures, including an especially prominent feature around 320 keV. The data have also been successful in extending (n, p_0) out to just below 10 MeV. The data for total (n, p) are extended up to 7 MeV, at which point contributions due to (n, np) start to become significant, along with other backgrounds. All together, the new measurements provide additional confidence in the scale of the cross section, confirming the issues with the current evaluations.

The results are also consistent with multiple measurements that derive the ^{35}Cl(n, p) cross section from measured CLYC detector efficiencies. Previous CLYC studies include Smith *et al.* [20], which derived cross sections for (n, p_0) in the energy range between 4 and 5.5 MeV and are consistent within uncertainty with our measurements. In the work of Warren [23], preliminary CLYC-derived cross section data are provided using the tandem-accelerator-driven neutron source at Ohio University. That work provides measurements of ^{35}Cl(n, p) in relation to ^{6}Li(n, t) and is in overall better agreement with the LANSCE data than with Ref. [21]. The trend

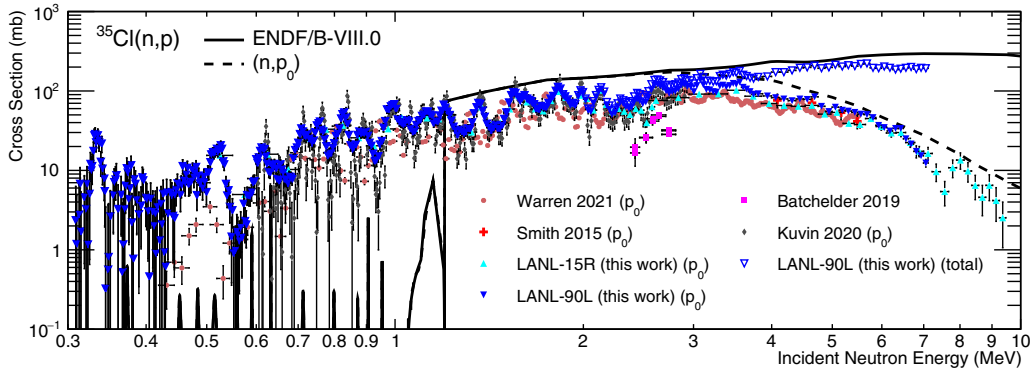

FIG. 4. Summary of newest data from WNR for ^{35}Cl(n, p) compared to available literature [1,20,21,23].

is very similar in terms of the observed fluctuations in the cross section; however, there exists a systematic energy shift between the resonances observed in their work and our own, visible in Fig. 4. The discrepancy between the resonances can be addressed through applying a time correction of approximately 8–12 ns that increases linearly with decreasing detected energy. Currently we attribute this to time-walk corrections that potentially needed to be made to the CLYC timing spectrum.

In Ref. [27], the efficiency of a CLYC detector was measured with a monoenergetic neutron source at approximately 1.5 MeV. The efficiency that is extracted is stated to be systematically lower than what is expected from using ^{35}Cl(n, p) cross sections from ENDF/B-VIII.0 and from the 2020 LANSCE measurement. However, in comparison with the 2020 LANSCE measurement, the authors referenced the energy averaged data point spanning a broad energy range 1.25–1.75 MeV of 61.4 mb. However, if the authors had compared the results with the finer-binned cross section data, which are provided in EXFOR, the cross section at 1.5 MeV is closer to 45 mb. With this cross section, the estimated CLYC efficiency at 1.5 MeV would be 0.154% instead of 0.21%, assuming a simple linear relationship from their study, compared to their measured 0.15%. Hence the measured efficiency is highly consistent with the LANSCE cross sections.

Finally, additional preliminary CLYC measurements recently performed at the University of California, Berkeley

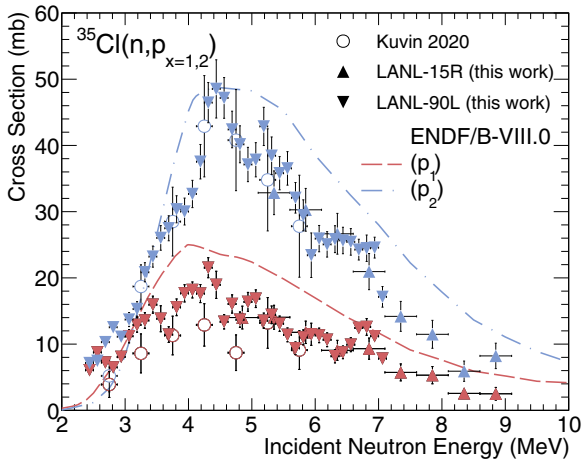

FIG. 5. Summary of newest data from WNR for ^{35}Cl(n, p_x) partial cross sections to ^{35}S excited states. Though not shown, data for $x = 3$, 4, and 5 were also collected and will be available in EXFOR.

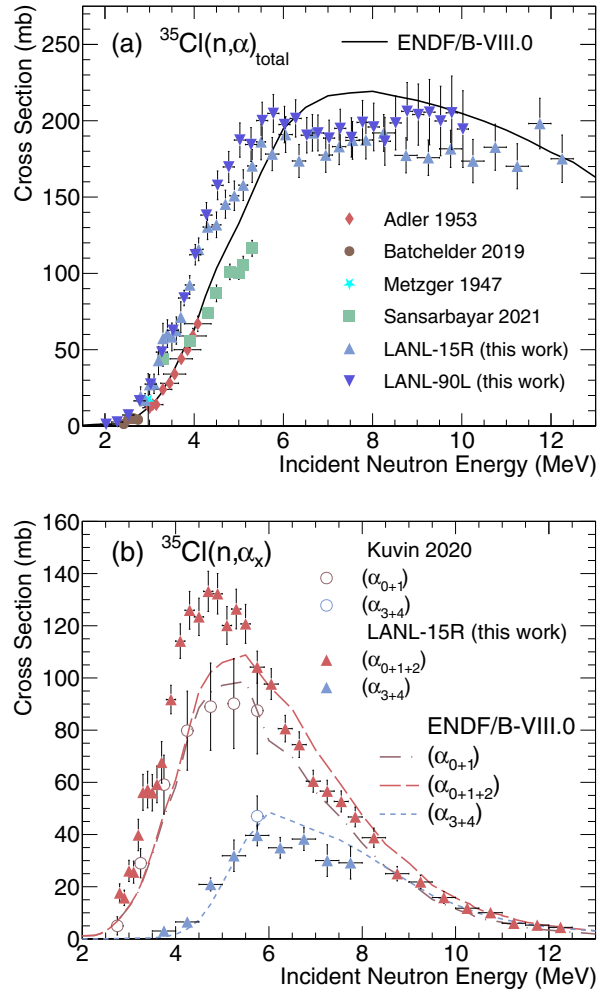

FIG. 6. Summary of newest data from WNR for ^{35}Cl(n, α) (a) total and (b) sums of partials to ^{32}P excited states, compared to unadjusted literature data [9,10,21,22] and ENDF/B-VIII.0.

appear to be generally consistent with the LANSCE measurements [28]. As a result, we consider the results of Batchelder *et al.* [21] to be an outlier, although the energy-dependent shape of the cross section is consistent when multiplied by a constant scaling factor of 250%.

2. *Data comparison:* ^{35}Cl$(n,\alpha)^{35}$S

The new LANSCE (n,α) cross sections are systematically higher than the evaluations along the rising edge of the cross section (below 6 MeV). This enhancement is measured in both the 15R and 90L data sets, which are consistent across nearly all energy bins. The central values are also slightly higher than the previous LANSCE measurement for (n,α_{0+1}), which is attributed to the influence of the strong background corrections needed in that work. Even so, the data are still consistent within 2σ due to the large systematic uncertainty assigned in that work from this source.

The scale of the evaluations in this energy range were defined primarily by the single measurement of Adler *et al.* from 1953 [10]. However, the Adler measurement was normalized relative to another old measurement of ^{14}N(n,α) and may not be as accurate as the uncertainties reflect. If instead recent evaluations of ^{14}N(n,α) cross section are used as a reference, the Adler cross sections may increase in scale by up to 20–40 % such that both the scale and trend of the Adler data are consistent with the LANSCE measurements. Therefore, for the sake of the reanalysis, a flat renormalization of +30% has been applied along with an additional 10% uncertainty (added in quadrature). The same is true of the Metzger *et al.* measurement [9] performed by the same group some years earlier, but due to its singular point and large error bars it was decided to leave this data out of the analysis and treat Adler as the final representation.

The LANSCE results are inconsistent with the recent work of Sansarbayar *et al.* [22], who measured a trend which was different from both Adler and our work. We identify the reason for their systematically larger data point at 3.4 MeV as being due to resonance contributions in the (n,α) cross section. This is reflected by an observed bump at this energy in the LANSCE measurement (see Fig. 6). So far, this is the only data point consistent between Ref. [22] and our work, therefore these data were not given significant weight in the following analysis.

Lastly, as mentioned for (n,p), the (n,α) measurement of Batchelder *et al.* [21] may also be as much as 250% too low, since it is possible that resonance structures observed from (n,p) are also manifesting in the (n,α) cross section at these energies.

There are no other experimental data to compare with the LANSCE ^{35}Cl(n,α) cross sections in the range between 6 and 12 MeV, although the trends are very consistent with that of ENDF/B-VIII.0 and extrapolating to the data of Verzilov *et al.* [29] and other measurements around 14 MeV. With the new measurements of ^{35}Cl(n,p) and ^{35}Cl(n,α) at LANSCE, we proceed with the reanalysis using statistical Hauser-Feshbach theory, incorporating all available experimental data for constraints.

III. ANALYSIS OF ^{35}Cl(n,X) AT FAST NEUTRON ENERGIES WITH HAUSER-FESHBACH THEORY

A. Overview

Given the data summarized above, we have reanalyzed the fast-energy (>100 keV) part of the ^{35}Cl system using statistical Hauser-Feshbach (HF) theory and coupled channels optical model potentials (OMPs). The challenges of applying this analysis to this mass range have already been mentioned, and can be seen in the discontinuous jump between R-matrix and HF approaches in the (n,p) cross section of ENDF/B-VIII.0 in Fig. 4. Nevertheless, as shown preliminarily in Ref. [1], the statistical calculations are still able to describe the average energy-dependent trends of the fluctuations, enough to serve as a prior for any finer adjustments. This section outlines this effort using the bulk of relevant and available experimental data, including those from LANSCE presented in Sec. II. To perform these calculations we employ the code COH$_3$ [30], the direct outputs of which are labeled throughout as LANL-TP-HF.

Adjustments to the proton, neutron, and α-particle OMPs (denoted n-OMP, p-OMP, and α-OMP from here on) were the starting point for the analysis, dominating the low-energy portions of the cross sections. Of the three, the n-OMP is the most impactful as it governs the dynamics of the entrance channel. To constrain this potential, literature data for the total cross section and elastic angular distributions on natural isotopes were used, followed by purely isotopic (n,p) and (n,α) data for the proton and α-particle OMPs, respectively. Global OMP sets from recent literature were utilized for each potential, as described in each section, with fractional adjustments linear in incident energy allowed up to a maximum of 25%, though the average adjustment did not exceed 5–10 %.

Once the cross sections in the low-energy region were well described by the OMPs, emphasis was put on the remaining components of the model to improve agreement at higher energies. These were primarily the level densities of residual nuclei (through the asymptotic parameter a^* of the Gilbert-Cameron parametrization) and the single-particle state densities of the exciton model for preequilibrium. Level density adjustments were constrained to no more than 10–15 % while state densities were not particularly constrained, being the most uncertain and at the extreme range of the present analysis.

B. Neutron OMP through scattering and ^{35}Cl$(n,$ total$)$

The adjustments to the neutron OMP presented in the previously published analysis [1] were investigated further to improve agreement with the ^{nat}Cl$(n,$ total$)$ data. Though the data were measured on natural abundance targets, the difference in calculations for ^{35}Cl and ^{37}Cl are negligible compared to the fluctuations; therefore tuning the isotopic calculation to the natural data was deemed sufficient. Once again the coupled-channels potential of Kunieda *et al.* [31] was used to account for deformation effects, using the finite-range droplet model parametrization of Ref. [32]. However, only the OMPs were adjusted in this work; the deformation parameters were held constant and only varied for the sake of uncertainty

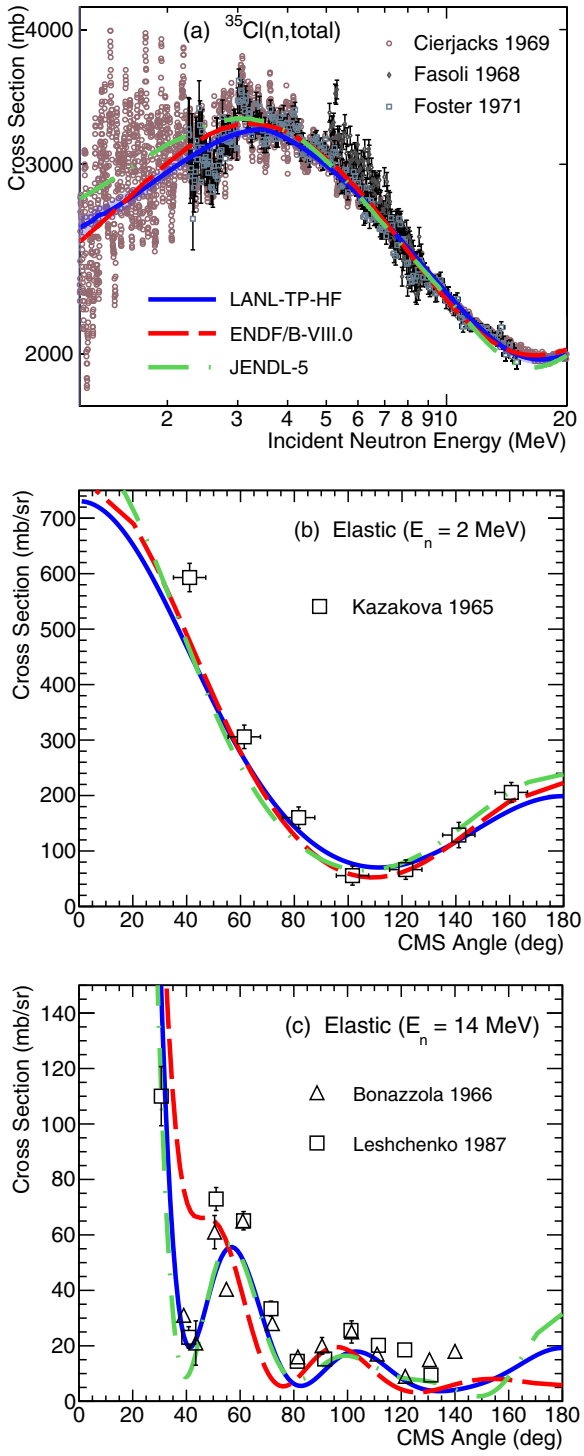

FIG. 7. (n, total) cross section (a) and elastic scattering angular distributions (b) and (c) in the energy region still described by statistical calculations. The calculations are for ^{35}Cl while the data are on natural targets: (a) [12–14], (b) [33], (c) [34,35].

quantification (Sec. IV). Further constraints were imposed with the inclusion of elastic scattering angular distributions at two energies in our range [33–35], also on natural targets. The cross sections are compared to current data in Fig. 7, and

TABLE III. Scaling factors applied to the OMPs of this work's Hauser-Feshbach calculations. The adjustments are linear in energy between the specified energy bounds and constant beyond. Lines indicate no adjustments were made.

Neutrons - Kunieda *et al.* 2007 [31] $0 \leqslant E \leqslant 3.5$ MeV						
	V	r_V	a_V	W_S	r_W	a_W
n_0	1.06	–	0.85	0.85	1.00	0.75
n_1	1.02	–	1.00	1.00	1.12	1.00
Protons - Kunieda *et al.* 2007 [31] $0 \leqslant E \leqslant 5.5$ MeV						
	V	r_V	a_V	W_S	r_W	a_W
p_0	1.06	1.10	0.75	–	–	–
p_1	1.02	1.05	1.00	–	–	–
α particles - Avrigeanu *et al.* 2014 [44] $5.0 \leqslant E \leqslant 10.0$ MeV						
	V	r_V	a_V	W_S	r_W	a_W
a_0	–	1.00	–	–	1.05	–
a_1	–	0.93	–	–	1.00	–

Table III presents a summary of the energy-dependent OMP adjustments.

Because of the (n, total) cross section's highly resonant behavior, these adjustments were not fit numerically but made by hand in order to reproduce the best statistical average of the data. The extra constraints provided by the scattering distributions proved crucial to this effort. Once a close manual description was achieved—for this and the remaining channels—the complete statistical calculations were run through a numerical Kalman filter [36], fitting all channels and data at once. Any systematic, robust, and physically relevant parameter adjustments made by the fit were evaluated and potentially reintroduced into the prior calculation. This process was repeated iteratively until a convergent solution was obtained, in which priors and posteriors for all channels and model parameters were within acceptable uncertainties of each other while still maintaining a physically appropriate model description. These convergent parameters are presented in the following tables.

One example of a major physics-based adjustment made to the n-OMP (which would be difficult to represent physically in the Kalman filter) is the reduction in neutron absorption due to structural effects in the compound nucleus. Because this change affected all subsequent model studies, it will be discussed further in the following section.

Reduction in neutron absorption

The optical model implicitly assumes that nuclear states in the vicinity of the excitation energy of the compound nucleus are well overlapped so that the absorption of incoming waves varies smoothly with energy. This situation is usually fulfilled for nucleon interactions with medium to heavy nuclei in the MeV energy range and higher. However, for the neutron induced reaction on ^{35}Cl, because of the large single-particle level spacing of ^{36}Cl near the Fermi surface in the neutron

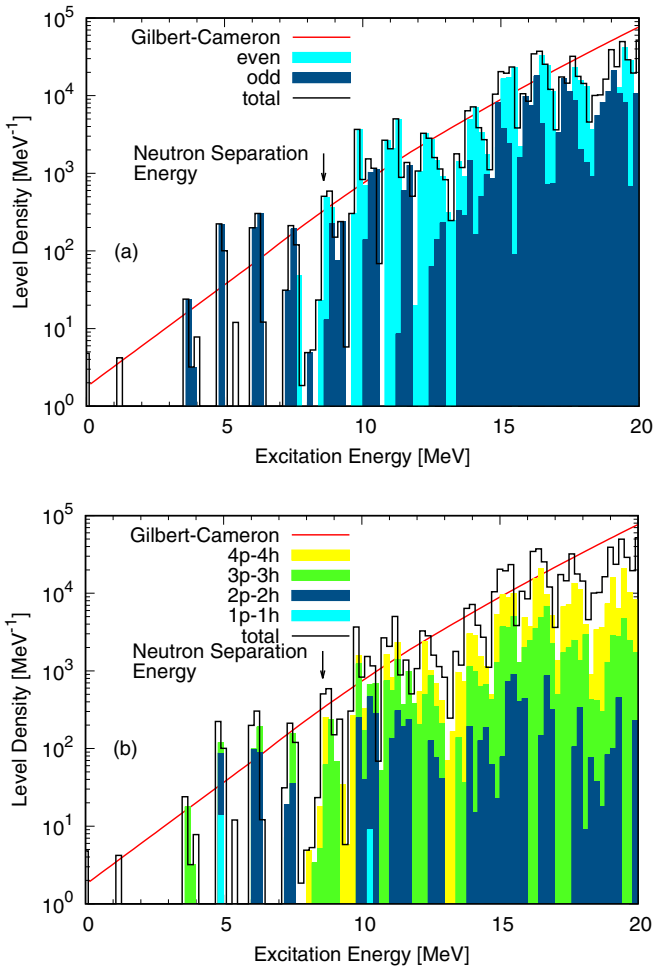

FIG. 8. Calculated level density of ^{36}Cl with the combinatorial technique based on the single-particle spectrum of FRDM. The top panel (a) shows the distribution of even and odd states in the total level density, and the bottom (b) shows the contribution from each particle-hole configuration up to $4p$-$4h$. The solid curve is the phenomenological model of Gilbert and Cameron.

shell, a strong nuclear structure effect may persist in the level density of the compound nucleus. Such a nonstatistical nature may cause a nucleus-specific energy dependence in the optical potential. To study the nuclear structure effect, we performed a combinatorial level density calculation for ^{36}Cl based on the single-particle spectrum by the finite range droplet model (FRDM) [32,37]. Unlike a large deformation seen in ^{35}Cl, FRDM predicts ^{36}Cl to be spherical. The combinatorial calculation includes the largest particle-hole configuration of $10p$-$10h$.

The last unoccupied neutron orbit is $0d_{3/2}$ (the binding energy of -11.7 MeV), which is about 5 MeV lower than the next orbit of $0f_{7/2}$ (-6.7 MeV). In addition, the next even-parity orbit $0g_{9/2}$ lies further. Due to the sparse single-particle spectrum, the level density of ^{36}Cl will be very low at low excitation energies, and they could be mostly odd parity states, as shown in Fig. 8(a). The phenomenological level density of Gilbert-Cameron [38] parameterized in COH$_3$ [39] is compared with the total level density. The bottom panel of Fig. 8 shows the decomposition of total level density into each of the particle-hole configurations up to $4p$-$4h$. Because of the large spacing of the single-particle orbits at the Fermi surface, the first $1p$-$1h$ state appears near 5 MeV.

When a few-MeV neutron interacts with ^{35}Cl, the compound nucleus is formed in the 10–15 MeV excitation energy range (the neutron separation energy is 8.58 MeV), and the strong fluctuation still remains in this energy range. Here we note that the combinatorial method for the level density calculation does not include any residual interactions that shift and broaden the eigenstate. Although the true level density should be smoother than the calculated level density with this technique, we can still make a qualitative argument. The noticeable dips near 11.5 and 13 MeV may prevent interacting neutrons forming a compound state, which results in a local energy dependence in the phenomenological optical potential. The absorption of incident neutrons is hindered, hence the compound nucleus cross sections into all the decay channels become smaller.

A similar argument can be made for the parity distribution. For the 2.5-MeV neutron incident on ^{35}Cl, the mainly contributing partial waves are s, p, d, and some f. Since the even-parity states predominantly distribute near 11 MeV, the p wave is strongly scattered rather than absorbed (the ground state of ^{35}Cl is $3/2^+$) due to fewer odd-parity states. This implies the optical potential may also reveal an angular momentum dependence [40]. A fully phenomenological determination of the optical potential by introducing local energy and angular momentum dependencies might be possible. However, we avoided this as it may lead into unphysical overfitting. Instead, we employed the Kunieda optical potential [31] as a base calculation, and reduced the absorption to reproduce the general tendency of the total cross section at low energies as done in our past study [1] but in a larger energy range.

C. OMPs for charged particle emission

1. Protons

As a starting point for the proton OMP, the parameter adjustments were set equal to those of the fitted neutron OMP, including the introduced linear energy dependence. This was to preserve isospin symmetry as much as possible. Any further adjustments to the OMP were then made as a result of fitting to the (n, p) channel data, first manually and then iteratively through the Kalman filter as described above. The results of these fits are shown in Table III for the OMP and Figs. 9 and 10 for the $(n, \mathrm{p})_{\mathrm{total}}$ and (n, p_0) cross sections, respectively.

For the sake of a consistent analysis, the data of Ref. [23] have been shifted in neutron energy by applying a time correction of 8–12 ns that increases linearly with decreasing neutron energy. The relative normalization of the points is then corrected based on the neutron flux information provided in the thesis, which also brings the CLYC-derived ^{6}Li(n, t) cross sections into better agreement with literature. With these adjustments the collective data line up extremely well across the observed resonant features. Despite these fluctuations, the statistical LANL-TP-HF calculation manages to describe the trends and averages well across the desired energy range,

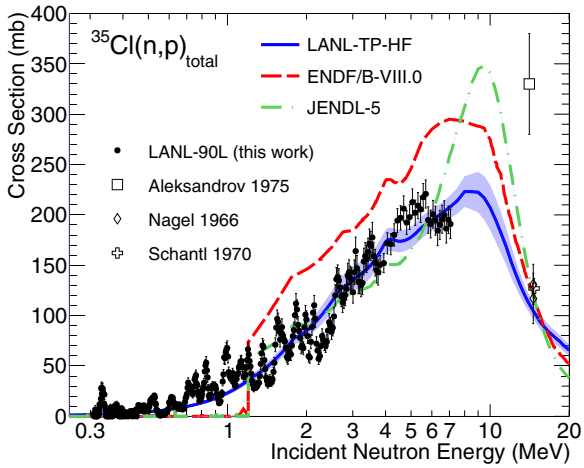

FIG. 9. Comparison of the LANL-TP-HF analysis (solid blue) for the total (n, p) cross section to ENDF/B-VIII.0 (dashed red) and JENDL-5 (dashed-dotted green). Also shown are higher-energy data from the literature: [41–43].

reinforcing the applicability of the Hauser-Feshbach analysis to this system.

Nevertheless, some of the fluctuations are significant enough that they may impact applications such as the MCRE. Therefore, the LANL-TP-HF calculation has been augmented by a direct fitting of the (n, p_0) data to catch the most macroscopic of these features. This is shown in Fig. 10 as the solid blue grouped cross section, that is this work's fitted statistical analysis and the R-matrix results of Ref. [6] combined. Not only does this better represent the measured data for this channel, but it also provides a solution to the 1.2 MeV discontinuity by adding the statistical results as background to the resonance analysis. Above 1.2 MeV, the principle adjustment compared to previous evaluations is an overall reduction in cross section by more than 30%, up to as high as 10 MeV. This grouped cross section is what will be available for use in the fully evaluated file.

For the sake of the uncertainty quantification, only the $(n, p)_{\text{total}}$ channel was passed through the Kalman filter, though the outlying datum of Aleksandrov *et al.* [41] was removed and those for Nagel [42] and Schantl [43] assigned 50% relative fitting weight. This was both to give preference to the lower-energy region of the cross section (more relevant for the MCRE and related systems) and also from questions of the absolute scale of these data, due to their lack of corrections for down-scattering effects typically important at these energies. To account for this, the Nagel and Schantl data were also reduced in absolute scale by 10%.

2. α particles

In the preliminary analysis in Ref. [1], only the (n, p) channel was adjusted to reproduce the observed reduction in cross section. For (n, α), the default α-particle optical model parameters from Avrigeanu *et al.* [44] were not adjusted to reproduce the experimental data and were on average higher than the measured cross sections.

As it happens, the new LANSCE measurements on this channel appear to be better reproduced by the default optical model parameters, rather than the adjustments required to have it match the scale of the unadjusted Adler data. It is worth noting that the use of the much older McFadden α-OMP [49] gives better agreement with the unadjusted Adler data. Hence switching between the two sets of global optical model parameters, of Avrigeanu and McFadden, appears to bound the available experimental data in this energy range. The (n, α) cross section for the present LANL-TP analysis is increased slightly at this leading edge, based on the LANSCE data and the corrected data of Adler (Fig. 11). This was done by a flat 5% increase in the imaginary radius of the Avrigeanu OMP up to 5 MeV (Table III). This particular adjustment was suggested by ^{35}Cl's being a well-deformed nucleus [32], which often modifies its geometry beyond the global models.

Any further fine tuning (ultimately to the real radius) was a result of the iterative Kalman filter process, primarily in the higher-energy region. In this region (> 10 MeV) the

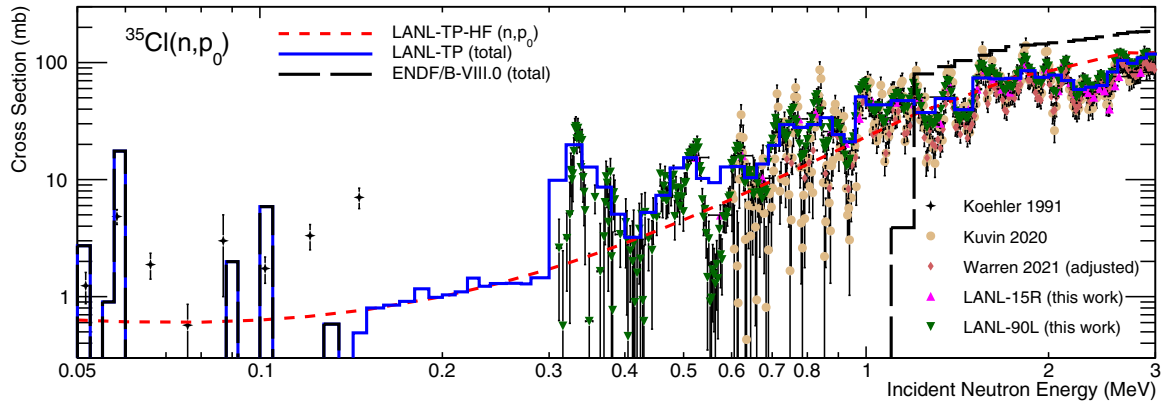

FIG. 10. Demonstration of the new LANL-TP calculations for ^{35}Cl(n, p), both the partial statistical LANL-TP-HF (n, p_0) (fine-dashed red) and the total (n, p) (solid blue) as a group cross section, i.e., including the resonance analysis. The Kalman uncertainties have not been plotted here for clarity. Comparison is again made to ENDF/B-VIII.0 (long-dashed black) to show the extension of this work's statistical cross section into the resonance region, where it has been added as background to the resonant cross section down to 140 keV. Literature data: [1,3,23].

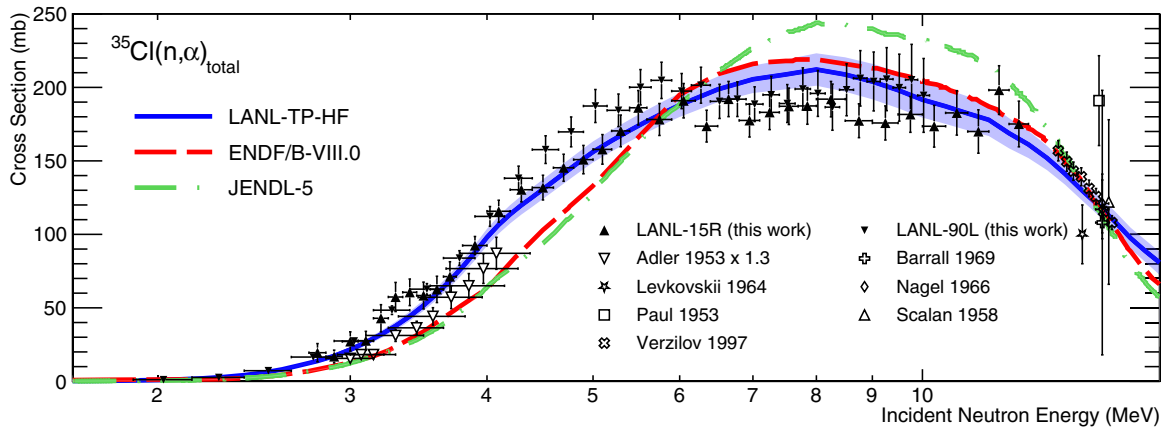

FIG. 11. Comparison of the LANL-TP-HF analysis (solid blue) for the total (n, α) cross section to ENDF/B-VIII.0 (dashed red) and JENDL-5 (dashed-dotted green). Also shown are other data from the literature: [10,29,42,45–48].

available data were not only sparser and more uncertain, but consistently lower than the default calculations. Similar to the (n, p) case, therefore, these data around ≈ 14 MeV were all assigned 50% relative fitting weight. However, by this point the level densities and pre-equilibrium effects begin to play more important roles; therefore these parameters became the new focus of the analysis.

D. Level densities and preequilibrium

In this work's energy range, the investigated cross sections were found to be most sensitive to the level densities (LDs) of three residual nuclei: ^{35}Cl, ^{35}S, and ^{32}P (from the (in)elastic, (n, p), and (n, α) channels, respectively). As mentioned, these level densities are implemented in COH$_3$ through the Gilbert-Cameron phenomenological model [38], which is modified through fractional adjustments to the asymptotic parameter a^*.

These adjustments take effect once the model switches over from reading discrete levels listed in the RIPL database [50]. (Where this switch happens is also adjustable in COH$_3$.) Typically this is around the high-energy mark defined earlier, with the most significant effects beyond 10 MeV.

Also in this region (though a bit higher, around 15 MeV) is where preequilibrium effects start to factor in. In COH$_3$ these enter through the two-component exciton model [51], where the relative strengths of the different particle emissions (neutrons, protons, or α particles) are controlled by fractional adjustments to the single-particle state densities (SDs). Therefore, all reliable data in the ^{35}Cl(n, X) channels around and above this region were fit predominantly using a combination of level density and preequilibrium adjustments.

A summary of the final adjustments are given in Table IV. These particular values were optimized by comparing manually to the existing data in the high-energy region for the (n, p) (Fig. 9), (n, α) (Fig. 11), and $(n, 2n)^m$ (Fig. 12) channels, the latter populating specifically the metastable first excited state of ^{34}Cl for which the data were most reliable. Like the OMP parameters, these were also run iteratively

TABLE IV. Fractional adjustments made to the asymptotic level density (a^*) and preequilibrium state density parameters relevant for this work. If applicable, the cutoff for discrete levels read in from RIPL is shown in parentheses.

asymp. level dens. (a^*)		pre-equilibrium	
^{35}Cl	1.15 (15)	proton	1.60
^{35}S	1.10 (15)	neutron	1.40
^{32}P	1.05	α part.	1.00

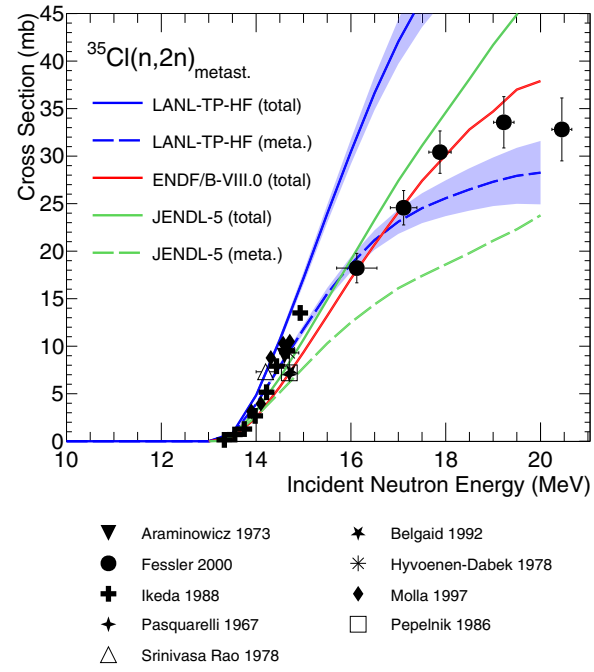

FIG. 12. Similar comparison for the $(n, 2n)$ reaction. The data shown [52–60] specifically populate the isomeric first excited state of ^{34}Cl; included, however, are calculations for both the isomeric final state (dashed) and total cross section (solid), to highlight discrepancies with previous evaluations.

through the same Kalman filter to find a final convergent set.

For the Gilbert-Cameron model, the best solution was found when the switch to statistical level density for both ^{35}Cl and ^{35}S was made around the fifteenth discrete level. This makes the (n, p) cross section sensitive to the LDs around 5 MeV in incident energy, where the distribution begins to peak. This change, along with a consistent 10–15 % increase in both LDs, was found to be necessary to match the trends of this work's new data while not neglecting the data around 14 MeV. It is also motivated by the fact that around the fifteenth level, the known properties of the levels of these two nuclei become more uncertain.

Beyond this energy, further constraints enter through the data on (n, α) and $(n, 2n)^m$, particularly the latter above 14 MeV ($Q = -12.6$ MeV). While this energy range is beyond the present work's immediate applications, care was still taken to ensure that good agreement was maintained across all three channels. To achieve this, large increases (of several tens of percent) to the preequilibrium single-particle SDs were found to be necessary, in addition to the LD and OMP adjustments discussed above. This is an effect that has been seen before in nuclei of this mass range [61].

The primary driver of these adjustments was the (n, p) channel. Of the three dataful channels, the (n, p) has the poorest data in the 14 MeV region, specifically in their lack of trend and high uncertainties. Nevertheless, the data are all consistently high in magnitude compared to what the statistical model alone would predict, suggesting the influence of other reaction mechanisms at these energies. Therefore, to maintain channel-wide agreement and the adjustments already made at lower energies, large increases in the preequilibrium strength were made to approximate these other potential reaction components. Future efforts include testing other reaction models, including more direct components, to see if this large adjustment can be better compensated.

It is worth noting that the present analysis increases the strength of the total $(n, 2n)$ channel by roughly 50% compared to previous evaluations. This appears to be because previous evaluations of $(n, 2n)$ have been matched to the data populating only the isomeric state in the residual. JENDL-5 reports the isomeric cross section independently while ENDF/B-VIII.0 has only the total. In the current analysis there is more consistent matching across all dataful channels in this energy region.

E. Special mention: Inelastic

Although an important reaction channel for the applications, the ^{35}Cl(n, n') cross section was not used to constrain the model in the present analysis. This was largely due to the paucity and low precision of available data. Reference [11] provides only partial inelastic scattering data inferred from γ-production cross sections off natural targets, the majority of which were not assigned uncertainties. The uncertainties that were provided were large enough to encompass all calculations, both published and of this work, and therefore were not constraining.

Nevertheless, the impact of this channel on the reanalysis could be significant, should more complete data be measured. At LANSCE, it would be feasible to perform new (n, n) and (n, n') scattering measurements on isotopically enriched samples of ^{35}Cl and ^{37}Cl using the CoGNAC detector array [62], as well as neutron transmission measurements at fast energies [63] and at intermediate energies with DICER [64]. Improved data on these channels at fast energies are a top requirement for future improvement on the model description.

F. Predictions for ^{37}Cl

The lessons learned from the analysis of ^{35}Cl also apply to ^{37}Cl, which has its own relevance in similar applications. Though a dedicated effort toward new measurements and reanalysis has yet to be applied to this isotope, the modifications to the model parameters informed by the data on ^{35}Cl have been checked against those available for ^{37}Cl, namely the OMP and preequilibrium components, which should more or less translate over. (Coupled channels effects have been removed, due to the lack of apparent deformation in this nucleus [32].) These comparisons have been made for ^{37}Cl(n, p) and (n, α) and are shown in Fig. 13 for a select subset of data pulled from EXFOR.

Despite the systematic discrepancy among certain data sets, there is still an average trend consistent with that of the various calculations. All the data shown are activation measurements from D-T neutron sources, hence their clustering around the 14 MeV region. Even so, combined with the (*n*, total) and (n, n) data presented above (which were for natural abundances) the data seem to encourage the broad model adjustments presented in this work; although preference cannot yet be given between ENDF/B and our present calculations, it is noteworthy that, for instance, the strong preequilibrium enhancement found necessary for ^{35}Cl appears to favor ^{37}Cl as well.

Nevertheless, more detailed comparisons are limited by the quality of the data, particularly the complete lack of it below 14 MeV (similar to the case of ^{35}Cl, until recently). Unlike ^{35}Cl, the (n, p) and (n, α) reactions on ^{37}Cl are threshold reactions due to their negative Q values, pushing the peak cross sections up toward higher energies. Still, measurements with LENZ with enriched targets are more than feasible to populate the cross section with brand new differential data at energies closer to threshold, which would be critical to constrain the calculations further. Such measurements are currently under consideration, as part of a full future reevaluation of the statistical region for ^{37}Cl, since such data will be crucial for reactor applications seeking to use salts enriched in ^{37}Cl.

IV. GENERATING MODEL UNCERTAINTIES

To obtain quantitative estimations of not just cross section uncertainties, but full cross-energy covariances, we utilized a Kalman filter on both the presented data and LANL-TP-HF. Using the LANL-TP-HF calculation as a prior, the (*n*, total), (n, p), (n, α), and $(n, 2n)^m$ channels were fit (in that order, from lowest energy to highest). Cross-energy correlations

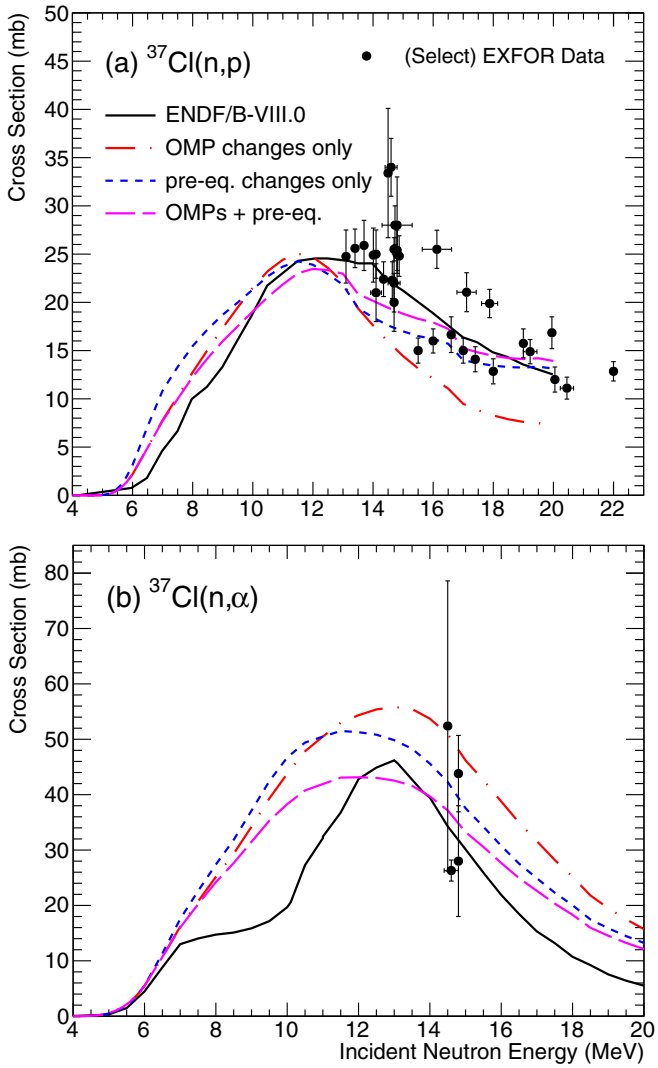

FIG. 13. A subset of the data for the (a) (n, p) and (b) (n, α) reactions on ^{37}Cl pulled from EXFOR. Shown in comparison are ENDF/B-VIII.0 (solid black) as well as three CoH calculations based on this work's adjustments for ^{35}Cl: only the OMP adjustments (dashed-dotted red), only the preequilibrium state density adjustments (short-dashed blue), and both together (long-dashed magenta). Data: (n, p) [43,47,48,53–55,58,61,65–68], (n, α) [47,48,66,69].

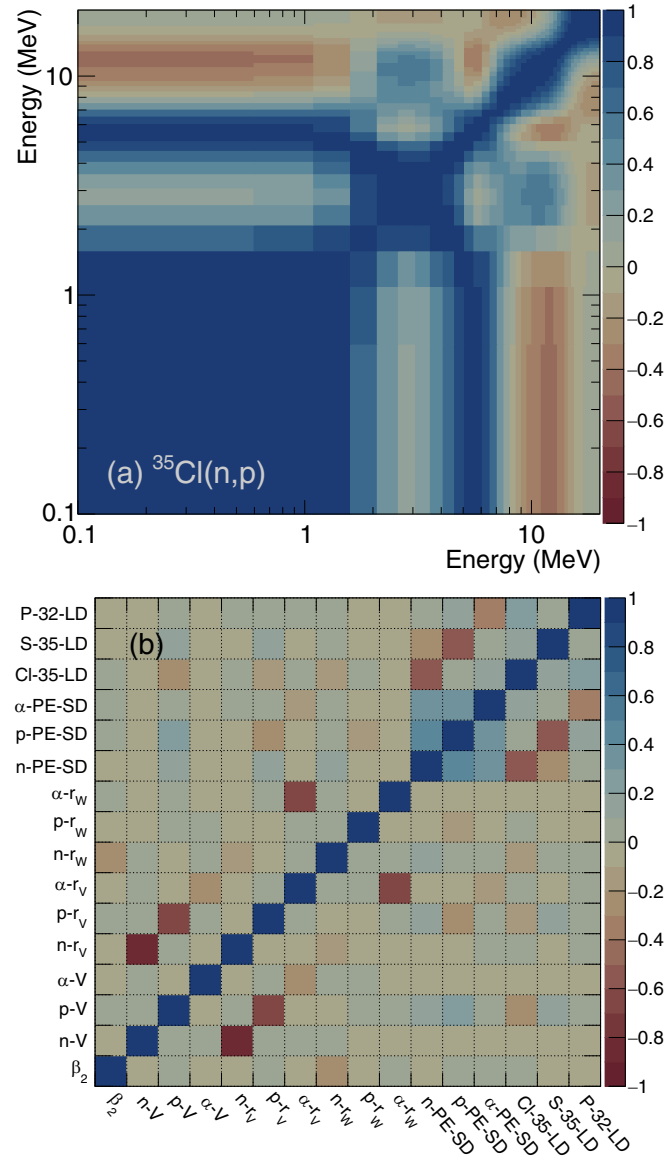

FIG. 14. Examples of correlation plots from the Kalman filter fitting: (a) ^{35}Cl(n, p), focused on the energy range of interest; (b) model correlations for the most sensitive parameters. In order (left-right or down-up) these are the dipole rotational deformation, real depths of each OMP, real and imaginary radii, particle state densities of the preequilibrium model, and the HF level densities for the principle residual nuclei. More parameters (imaginary OMP depths, OMP diffusenesses, higher-order deformations) were included in the ultimate fit, but were low in sensitivity and therefore left out of the plot for conciseness.

within single channels were allowed based on perturbative model parameter sensitivities, but not cross-channel correlations. The criteria for a good fit were that (i) the LANL-TP-HF prior and the fitted posterior calculations lie within uncertainty of one another and (ii) the fitted model parameters do not stray outside their preset uncertainties. Until these criteria were reached, this procedure was performed iteratively, manually adjusting the input LANL-TP-HF each time based on the fit results.

The resulting fit uncertainties (applied to the prior LANL-TP-HF as relative values) are the blue uncertainty bands in Figs. 7, 9–12. An example of the fit correlations for the (n, p) channel is shown in Fig. 14(a), along with the correlations among principle model parameters [Fig. 14(b)]. In the (n, p) correlations, the influence of the different models as they come in at different energies can be distinguished, e.g., the level densities at few MeV and the preequilibrium above 10 MeV. These features are reinforced by the model correlations, which show the strong but largely independent cross correlations between OMP parameters and between LDs and SDs, each in their own blocks. These features played heavily into the energy-dependent analysis process described above,

starting first with OMPs and adding in other components as they became relevant.

Not all data shown above were included in the fit, and not all with uniform weights. A summary of the data included and their assigned weights is presented in Appendix A. These decisions—which data to include in the analysis, and which to generate uncertainties—were made using the authors' judgment, and typically came down to consistency across measurements and reliability in the methods and reference reactions applied, as already discussed for certain data sets.

V. DISCUSSION

In Sec. II, we reported new differential experimental data for the (n, p) and (n, α) neutron absorption cross sections to constrain the theoretical analysis of the $^{35}\mathrm{Cl}(n, X)$ system, as presented in Sec. III. In this section, consistency is found between the evaluated cross sections and a variety of other sources such as CLYC-efficiency-derived $^{35}\mathrm{Cl}(n, p_0)$ cross sections, integral spectrum averaged data for $^{35}\mathrm{Cl}(n, \alpha)$ from D-T fusion applications [29], and fission spectrum averaged cross sections for $^{35}\mathrm{Cl}(n, \alpha)$ and $^{37}\mathrm{Cl}(n, p)$. No criticality benchmarks exist for chlorine nuclear data at fast energies, but some efforts are being planned. The improved knowledge on the excitation function of the (n, p) cross section will help to understand the sensitivities for planning those experiments. In general, fission spectrum averaged cross sections on $^{35}\mathrm{Cl}(n, p)$ are lacking due to the fact that (n, p) is not a threshold reaction and has a relatively large cross section at thermal energies, which makes it very sensitive to the method used to isolate the contributions from the pure fission spectrum from the background.

A. CLYC detector efficiency

The use of Cs_2LiYCl_6:Ce (CLYC) and other similar chlorine-based detectors are being extensively explored for use in a variety of applications, particularly for neutron spectroscopy in nuclear physics experiments [70] and as neutron flux monitors in D-D generators [71]. For these applications, the fluctuations in the $^{35}\mathrm{Cl}(n, p)$ cross section need to be considered carefully. For example, in the 2–3 MeV range important for monitoring the flux of neutrons produced by D-D fusion, the measured cross section exhibits a prominent dip by multiple factors and varies dramatically around 2.6 MeV (see Fig. 10). For studies of (d, n) reactions in inverse kinematics near the Coulomb barrier at radioactive ion beam facilities, the outgoing neutron energies of interest are typically between 100 keV to a few MeV. Hence, a narrow state populated by (d, n) could go undetected or be significantly enhanced depending on the overlap with the competing resonances in this energy range. For this reason, it is recommended that the cross sections used in such applications be those in which the fluctuations have been in some way accounted for, such as the grouped LANL-TP cross section in Fig. 10, which will be available in a fully evaluated file.

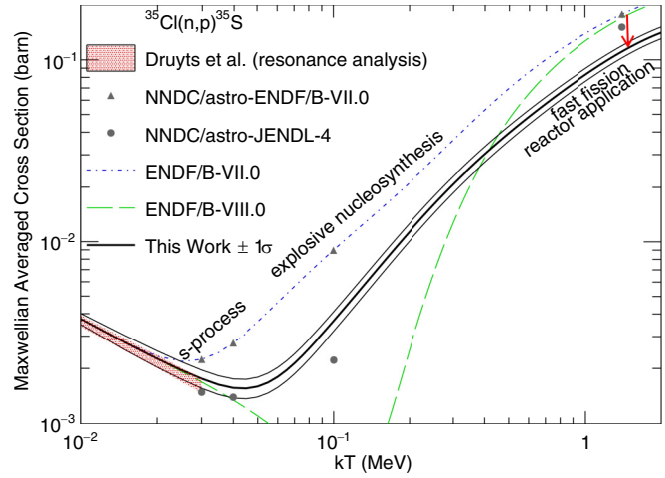

FIG. 15. Calculated MACS from ENDF/B-VII.0 (blue dash-dot line), ENDF/B-VIII.0 (green long-dash line), and the experimentally constrained values from this work (black line). The blue curve is benchmarked against the values available on the NNDC web site as a consistency check for the method used to integrate the point-wise cross sections. Regions of interest for *s*-process and explosive nucleosynthesis for nuclear astrophysics, and for the fast fission reactor applications, are labeled.

B. Maxwellian-averaged cross sections (MACS) and reaction rates

In contrast to the aforementioned application, applications of nuclear data for nuclear astrophysics or criticality calculations for reactor applications are more interested in average reaction rates that are derived from the average cross section in a particular neutron spectrum. To model this, the average cross sections are calculated assuming neutron energies that follow a Maxwellian distribution as a function of temperature.

Here we calculate the Maxwellian-averaged cross sections (MACS) for several evaluations including this work's, following the Simpson method for neutron induced reactions [72]. The results are shown in Fig. 15 and are benchmarked against calculations performed using available nuclear data from the NNDC. At the temperatures most relevant to understand the potential production of ^{36}Cl and ^{36}S in the galaxy through *s*-process and explosive nucleosynthesis, between 0.3–2 GK ($kT = 25$ to 200 keV), the reaction rates vary significantly between ENDF/B-VII.0, ENDF/B-VIII.0, and this work. However, the experimentally constrained rates from this work are in good agreement with standard reaction libraries that are used for nuclear astrophysics. For example, good agreement is found, within 20% at energies between 0.3 and 2 GK, with the NON-SMOKER statistical reaction rate calculations obtained from REACLIB [73]. Above and below these energies the calculations diverge, with the current evaluated rates matching well with the rates of Druyts *et al.* at low energy, due to the previous resonance analysis up to 100 keV [6] that is adopted without adjustment, and with the LANSCE experimental data at higher temperatures. The current rates are just outside the 1σ bands of the TENDL-2023-astro rates that are based on 480 model variations of TALYS statistical model calculations. This discrepancy is explained by the necessary

adjustments to reduce absorption proposed in this work, which have not been implemented in the TALYS calculations.

As the temperature is increased up to $kT \simeq 1.4$ MeV, relevant for fast fission applications such as the MCRE, the precision needs are much higher than what are typically needed for nuclear astrophysics. The change between ENDF/B-VII.0, ENDF/B-VIII.0 and this work is a dramatic reduction in the absorption cross section, as highlighted by the red arrow in Fig. 15. The impact of this is more neutrons left in the system, resulting in an overall increase in reactivity for a fast reactor. Although not discussed here in detail, other impacts are in the inventory of radioactive nuclei, for which (n, p) and (n, γ) reactions produce short-lived ^{35}S and long-lived ^{36}Cl ($T_{1/2} \approx 300$ ky).

C. Fast fission spectrum-averaged cross sections (SACS)

As previously mentioned, integral measurements of fission spectrum-averaged cross sections on ^{35}Cl(n, p) are lacking. There are some references for ^{35}Cl(n, α) SACS in the literature, though they are all decades old with reported values spreading from as low as 3 mb to as high as 44 mb, most with no uncertainties provided. Evaluations of the SACS have attempted to make consistent corrections based on other monitor or reference reactions, but are not very reliable. References [74] and [75] are the only papers with uncertainties quoted; however, they are still not ideal due to lack of adequate information regarding the shape of the neutron flux.

Hence, additional differential-integral measurements of ^{35}Cl$(n, \alpha)^{32}$P could be made to tune the rise from threshold for this reaction channel. For now, the weighted average of the measured SACS from Pfrepper and Hayodom are 24.3 ± 1 mb. This compares to the derived SACS from our differential cross section measurements, folded with a ^{235}U Watt spectrum, of 23.4 ± 1.3 mb. The value derived from the ENDF/B-VIII.0 cross section is 19.4 mb. This change will result in a non-negligible increase to the neutron absorption in fast spectrum reactors, but the sensitivity is much smaller compared to the scale of (n, p) in the energy range between 600 keV and 2 MeV. For ^{37}Cl$(n, p)^{37}$S, the most recent measurements are from Refs. [76] and [77] who obtain consistent fission spectrum average cross sections of about 0.22 ± 0.02 mb, which compares to the current COH calculated value of 0.24 mb. This comparison shows the overall better consistency between the new statistical calculations across both stable chlorine isotopes.

D. D-T fusion benchmarks and dosimetry

As the incident neutron energy is increased up to and above 14 MeV, the cross sections become important for D-T fusion applications. In Ref. [29], the authors report differential-integral measurements which provide direct constraints for the ^{35}Cl(n, α) cross sections around 13–15 MeV and then indirect constraints for the trend of the cross section down to lower energies through measured spectrum-averaged cross sections in a beryllium moderating assembly. Comparisons of the evaluations to available experimental data tend to neglect showing the work of Verzilov because it was not included in EXFOR at the time of this publication. However, it appears that the ENDF and JENDL evaluations were heavily informed by this measurement. A preliminary reanalysis of the integral data from that work indicates that the current evaluation performs equally as well as ENDF/B-VIII.0, within the estimated 10–20 % uncertainty inferred from the measured C/E ratios of the monitor reactions. The discrepancies observed in the monitor reactions likely indicate some uncertainty in the neutron spectra simulated for each depth in the beryllium assembly. Excellent agreement to the integral data is observed at the position closest to the D-T neutron source, as all evaluations match well with the differential data of Verzilov [29].

Aside from (n, α), there are a few other important reactions for D-T fusion applications including ^{35}Cl$(n, 2n)^{34m}$Cl and ^{37}Cl$(n, 2n)^{36}$Cl. The former is identified as a potential monitor reaction for dosimetry applications, whereas the latter contributes to the production of long-lived ^{36}Cl and is a potential waste concern if chloride-salt-based tritium breeder blankets are considered [78]. An analogous question then exists to the pros/cons of ^{37}Cl enrichment in the molten-chloride fast-reactor application to reduce the production of ^{35}S from (n, p) and ^{36}Cl from (n, γ). Hence, as discussed in Ref. [78], the improved predictions that come out of this work, although focused on fast fission spectrum applications, will also benefit fusion energy applications of nuclear data.

VI. SUMMARY AND CONCLUSION

To address the urgent nuclear data needs of the next-generation fast spectrum reactor community, a targeted campaign to reduce the uncertainties associated with the knowledge of ^{35}Cl(n, X) reactions was performed. This effort involved the analysis of available experimental data, covering different reaction channels and incident neutron energies, within a statistical Hauser-Feshbach framework aided through new LANSCE measurements to constrain the (n, p) and (n, α) reaction channels. Within the scope of this project, particular emphasis was placed on improving the knowledge within the region of highest sensitivity to the MCRE. As part of this, new uncertainty and covariance information are provided at incident neutron energies above 1.2 MeV, where none were previously available in ENDF/B-VIII.0.

The challenges of reaction modeling in this mass range were discussed, though it was shown that statistical Hauser-Feshbach is able to capture the average energy trends of the cross sections above 100 keV, in spite of significant fluctuations. Hence, the Hauser-Feshbach approach is still a valid and useful tool for studying systems where many reaction channels may be open and to test the nuclear physics inputs that simultaneously affect the different emission probabilities.

The improved knowledge of the ^{35}Cl(n, p) reaction cross section, supported by new LANSCE measurements, significantly improves the accuracy and precision of criticality calculations for the MCRE and other fast spectrum applications that employ chloride salts [79]. Another major impact is on the simulated detector response of CLYC detectors, particularly ^{6}Li-depleted CLYC, for which the simulated efficiency significantly increases below 1.2 MeV and decreases above 1.2 MeV, if the current evaluation is used as an input. The

fluctuations in the cross section are critical for applications that plan to use CLYC detectors for neutron spectroscopy in nuclear physics measurements [70] or as a neutron monitor at D-D fusion neutron generators [71].

To validate, benchmark, and improve the precision further on this analysis and other future evaluations of chlorine data, it is recommended for integral measurements to be performed that are sensitive to fast neutron energies. Although (n, p) was identified as the most impacting reaction to constrain for the near-term goals of the Molten Chloride Reactor Experiment and other similar efforts, differential measurements on other reaction channels like (n, n'), for which experimental data are still lacking, are needed to achieve the precision goals for further commercialization.

ACKNOWLEDGMENTS

This work benefits from the LANSCE accelerator facility and was supported by the US Department of Energy Office of Nuclear Energy/Gateway for Accelerated Innovation in Nuclear (GAIN) voucher NE-22-28590 and a Cooperative Research and Development Agreement (CRADA) with TerraPower LLC. This work was carried out under the auspices of the National Nuclear Security Administration of the US Department of Energy at Los Alamos National Laboratory under Contract No. 89233218CNA000001. The isotopes used in this research were supplied by the US Department of Energy Isotope Program, managed by the Office of Isotope R&D and Production. The authors would like to thank Khachatur Manukyan, of Notre Dame, for performing the target fabrication and initial characterization, and David Ingram and Alexander Voinov of Ohio University for additional target characterization using the Ohio Tandem Accelerator Facility. We thank Lukas Zavorka, of Oak Ridge National Laboratory, for continued support with MCNP simulations using updated LANL evaluations. Through small workshops organized by TerraPower LLC, we acknowledge the useful discussions between other producers of chlorine nuclear data, including Lee Bernstein and Tyler Nagel from the University of California, Berkeley; Justin Warren, Alexander Voinov, and Carl Brune from Ohio University; Javier Praena from the Universidad de Granada, Spain; and Marco Pigni from Oak Ridge National Laboratory. We also acknowledge Jesse Brown, from Oak Ridge National Laboratory, for fruitful discussions ahead of a Nuclear Criticality Safety Program (NCSP) collaboration to further improve the description of chlorine nuclear data in the resolved resonance region. Finally, we thank Amy Lovell, Ionel Stetcu, and Wim Haeck, of LANL, for the implementation of the Kalman Filter method and with NJOY processing.

APPENDIX A: DATA USED FOR UNCERTAINTY QUANTIFICATION (Kalman filter)

A summary of data sets included in the Kalman filter for model optimization and uncertainty quantification is given in Table V. These selections were made in order to provide a stable fit within a physically reasonable model space without overconstraining (underestimating) the resultant uncertainties. Weighted preference was also given to data in the energy range most relevant for the MCRE, reflecting the uncertainty in the quality of the higher-energy data discussed in the main text. In general, the toggling of these weights (from 0.5–1.0) affected mainly the widths of the uncertainty bands, less the actual centroids of the calculations (which were more constrained by the uncertainty bounds of the model parameters, and overall remained within uncertainty of the priors).

TABLE V. Summary of data sets included in the Kalman filter for model optimization and uncertainty quantification. References with absolute scales or uncertainties modified from the original are indicated with a (*), the details of which can be found in the main text. A weight of 1.0 indicates no change to the reference uncertainties at the fit stage.

		Ref.	Weight
(n, total)			
	Cier69	[12]	1.0
	Faso68	[13]	1.0
	Fost71	[14]	1.0
	Sing74	[15]	1.0
(n, p)			
	LANL-90L	this work	1.0
	*Nage66	[42]	0.5
	*Scha70	[43]	0.5
(n, α)			
	LANL-90L	this work	1.0
	LANL-15R	this work	1.0
	*Adle53	[10]	1.0
	Barr69	[46]	0.5
	Levk64	[45]	0.5
	Nage66	[42]	0.5
	Paul53	[47]	0.5
	Scal58	[48]	0.5
	Verz97	[29]	0.5
$(n, 2n)^m$			
	Aram73	[52]	1.0
	Belg92	[53]	1.0
	Fess00	[54]	1.0
	Hyvo78	[55]	1.0
	Iked88	[56]	1.0
	Moll97	[57]	1.0
	Pasq67	[58]	1.0
	Pepe86	[59]	1.0
	Srin78	[60]	1.0

The output of the analysis in the form of an evaluated nuclear data file (ENDF) will be hosted by the National Nuclear Data Center. Please contact the authors for more information.

APPENDIX B: TABLES OF MEASURED (n, p) and (n, α) CROSS SECTIONS

The measured cross sections for (n, p_{total}) and $(n, \alpha_{\text{total}})$ at the 90L ($\Delta L = 8.2$ m) and 15R ($\Delta L = 15.2$ m) flight paths are provided in Tables VI–VIII.

TABLE VI. Measured cross sections for (n, p_{total}).

E_n (MeV)	ΔE_n (MeV)	$\sigma^{\pm\text{stat}}_{\pm\text{sys}}$ (mb)
0.3115	0.0029	$2.60^{\pm1.92}_{\pm0.21}$
0.3161	0.0018	$0.56^{\pm1.86}_{\pm0.05}$
0.3209	0.003	$3.15^{\pm1.97}_{\pm0.26}$
0.3246	0.0006	$5.03^{\pm4.31}_{\pm0.41}$
0.3258	0.0006	$12.00^{\pm4.60}_{\pm0.97}$
0.3271	0.0006	$9.97^{\pm4.70}_{\pm0.81}$
0.3283	0.0006	$11.22^{\pm4.53}_{\pm0.91}$
0.3296	0.0006	$17.46^{\pm4.99}_{\pm1.41}$
0.3309	0.0006	$27.47^{\pm5.17}_{\pm2.23}$
0.3321	0.0006	$28.50^{\pm5.30}_{\pm2.31}$
0.3334	0.0006	$22.34^{\pm5.21}_{\pm1.81}$
0.3347	0.0006	$27.51^{\pm5.17}_{\pm2.23}$
0.336	0.0006	$23.94^{\pm4.73}_{\pm1.94}$
0.3373	0.0007	$22.55^{\pm4.92}_{\pm1.82}$
0.3386	0.0007	$12.70^{\pm4.25}_{\pm1.03}$
0.3399	0.0007	$21.63^{\pm4.74}_{\pm1.75}$
0.3413	0.0007	$10.42^{\pm3.81}_{\pm0.84}$
0.3426	0.0007	$7.80^{\pm3.62}_{\pm0.63}$
0.3439	0.0007	$5.44^{\pm3.44}_{\pm0.44}$
0.3494	0.0048	$0.62^{\pm1.68}_{\pm0.05}$
0.3571	0.0028	$7.05^{\pm1.80}_{\pm0.57}$
0.3643	0.0044	$1.64^{\pm2.51}_{\pm0.13}$
0.3695	0.0007	$3.25^{\pm3.36}_{\pm0.26}$
0.371	0.0008	$6.38^{\pm3.48}_{\pm0.51}$
0.3725	0.0008	$10.60^{\pm3.56}_{\pm0.85}$
0.3741	0.0008	$9.34^{\pm3.40}_{\pm0.75}$
0.3756	0.0008	$4.33^{\pm3.12}_{\pm0.35}$
0.3771	0.0008	$5.93^{\pm3.25}_{\pm0.48}$
0.3787	0.0008	$11.60^{\pm3.31}_{\pm0.94}$
0.3802	0.0008	$2.20^{\pm2.83}_{\pm0.18}$
0.3818	0.0008	$0.76^{\pm2.73}_{\pm0.06}$
0.3834	0.0008	$7.74^{\pm3.05}_{\pm0.62}$
0.385	0.0008	$6.74^{\pm3.03}_{\pm0.54}$
0.3931	0.0074	$3.40^{\pm1.56}_{\pm0.27}$
0.4014	0.0008	$4.30^{\pm2.46}_{\pm0.35}$
0.4031	0.0009	$3.06^{\pm2.29}_{\pm0.25}$
0.4048	0.0009	$0.46^{\pm2.28}_{\pm0.04}$
0.4083	0.0026	$2.47^{\pm1.52}_{\pm0.20}$
0.4118	0.0009	$2.00^{\pm2.37}_{\pm0.16}$
0.4136	0.0009	$2.82^{\pm2.60}_{\pm0.23}$
0.4154	0.0009	$0.89^{\pm2.31}_{\pm0.07}$
0.419	0.0027	$1.59^{\pm1.50}_{\pm0.13}$
0.4226	0.0009	$3.78^{\pm2.42}_{\pm0.30}$
0.4244	0.0009	$2.10^{\pm2.38}_{\pm0.17}$
0.4263	0.0009	$5.05^{\pm2.40}_{\pm0.41}$

TABLE VI. (*Continued.*)

E_n (MeV)	ΔE_n (MeV)	$\sigma^{\pm\text{stat}}_{\pm\text{sys}}$ (mb)
0.4281	0.0009	$0.93^{\pm2.10}_{\pm0.07}$
0.43	0.0009	$0.62^{\pm2.05}_{\pm0.05}$
0.4319	0.0009	$5.26^{\pm2.39}_{\pm0.42}$
0.4377	0.0048	$3.13^{\pm1.41}_{\pm0.25}$
0.4435	0.001	$2.49^{\pm1.90}_{\pm0.20}$
0.4455	0.001	$4.89^{\pm2.01}_{\pm0.39}$
0.4515	0.0051	$4.78^{\pm1.36}_{\pm0.38}$
0.4576	0.001	$11.20^{\pm2.16}_{\pm0.90}$
0.4597	0.001	$7.41^{\pm1.95}_{\pm0.59}$
0.4618	0.001	$6.94^{\pm2.09}_{\pm0.55}$
0.4639	0.0011	$8.80^{\pm2.03}_{\pm0.70}$
0.466	0.0011	$10.65^{\pm2.12}_{\pm0.85}$
0.4681	0.0011	$6.62^{\pm1.87}_{\pm0.53}$
0.4703	0.0011	$6.74^{\pm1.87}_{\pm0.54}$
0.4724	0.0011	$7.26^{\pm2.00}_{\pm0.58}$
0.4746	0.0011	$10.10^{\pm2.09}_{\pm0.81}$
0.4768	0.0011	$8.15^{\pm2.02}_{\pm0.65}$
0.479	0.0011	$9.18^{\pm1.95}_{\pm0.73}$
0.4812	0.0011	$10.93^{\pm2.07}_{\pm0.87}$
0.4835	0.0011	$4.85^{\pm1.71}_{\pm0.39}$
0.4857	0.0011	$8.50^{\pm1.97}_{\pm0.68}$
0.488	0.0011	$6.80^{\pm1.88}_{\pm0.54}$
0.4903	0.0011	$7.20^{\pm1.77}_{\pm0.57}$
0.4926	0.0012	$5.92^{\pm1.68}_{\pm0.47}$
0.4949	0.0012	$8.38^{\pm1.79}_{\pm0.67}$
0.4972	0.0012	$7.12^{\pm1.68}_{\pm0.57}$
0.4996	0.0012	$5.33^{\pm1.61}_{\pm0.42}$
0.5019	0.0012	$9.41^{\pm1.79}_{\pm0.75}$
0.5043	0.0012	$9.47^{\pm1.77}_{\pm0.75}$
0.5067	0.0012	$12.62^{\pm1.88}_{\pm1.00}$
0.5091	0.0012	$15.77^{\pm2.06}_{\pm1.25}$
0.5116	0.0012	$16.84^{\pm2.06}_{\pm1.34}$
0.514	0.0012	$16.23^{\pm2.08}_{\pm1.29}$
0.5165	0.0012	$17.15^{\pm2.05}_{\pm1.36}$
0.519	0.0012	$18.63^{\pm2.11}_{\pm1.48}$
0.5215	0.0013	$17.12^{\pm2.05}_{\pm1.36}$
0.524	0.0013	$18.25^{\pm2.19}_{\pm1.45}$
0.5265	0.0013	$20.69^{\pm2.22}_{\pm1.64}$
0.5291	0.0013	$18.68^{\pm2.07}_{\pm1.48}$
0.5317	0.0013	$12.95^{\pm1.81}_{\pm1.03}$
0.5343	0.0013	$11.77^{\pm1.77}_{\pm0.93}$
0.5369	0.0013	$6.74^{\pm1.51}_{\pm0.53}$
0.5395	0.0013	$4.79^{\pm1.38}_{\pm0.38}$
0.5422	0.0013	$5.57^{\pm1.43}_{\pm0.44}$
0.5448	0.0013	$3.47^{\pm1.27}_{\pm0.28}$

TABLE VI. (*Continued.*)

E_n (MeV)	ΔE_n (MeV)	$\sigma^{\pm\text{stat}}_{\pm\text{sys}}$ (mb)
0.5475	0.0014	$1.46^{\pm1.08}_{\pm0.12}$
0.5503	0.0014	$3.13^{\pm1.22}_{\pm0.25}$
0.553	0.0014	$0.90^{\pm1.01}_{\pm0.07}$
0.5557	0.0014	$0.97^{\pm0.99}_{\pm0.08}$
0.5585	0.0014	$1.70^{\pm1.05}_{\pm0.13}$
0.5613	0.0014	$1.54^{\pm1.01}_{\pm0.12}$
0.5641	0.0014	$1.29^{\pm0.99}_{\pm0.10}$
0.567	0.0014	$1.89^{\pm1.09}_{\pm0.15}$
0.5698	0.0014	$1.43^{\pm0.96}_{\pm0.11}$
0.5727	0.0014	$3.76^{\pm1.14}_{\pm0.30}$
0.5756	0.0015	$2.28^{\pm1.05}_{\pm0.18}$
0.5785	0.0015	$2.07^{\pm1.00}_{\pm0.16}$
0.5815	0.0015	$4.85^{\pm1.20}_{\pm0.38}$
0.5845	0.0015	$4.81^{\pm1.21}_{\pm0.38}$
0.5875	0.0015	$4.76^{\pm1.16}_{\pm0.38}$
0.5905	0.0015	$5.28^{\pm1.17}_{\pm0.42}$
0.5935	0.0015	$7.00^{\pm1.29}_{\pm0.55}$
0.5966	0.0015	$7.25^{\pm1.32}_{\pm0.57}$
0.5997	0.0015	$13.76^{\pm1.61}_{\pm1.08}$
0.6028	0.0016	$12.32^{\pm1.58}_{\pm0.97}$
0.6059	0.0016	$14.53^{\pm1.63}_{\pm1.14}$
0.6091	0.0016	$17.49^{\pm1.75}_{\pm1.38}$
0.6123	0.0016	$19.26^{\pm1.84}_{\pm1.52}$
0.6155	0.0016	$18.65^{\pm1.87}_{\pm1.47}$
0.6187	0.0016	$18.37^{\pm1.82}_{\pm1.44}$
0.622	0.0016	$14.98^{\pm1.64}_{\pm1.18}$
0.6252	0.0016	$12.21^{\pm1.50}_{\pm0.96}$
0.6286	0.0017	$9.61^{\pm1.36}_{\pm0.76}$
0.6319	0.0017	$9.33^{\pm1.32}_{\pm0.73}$
0.6353	0.0017	$11.88^{\pm1.47}_{\pm0.93}$
0.6387	0.0017	$10.57^{\pm1.42}_{\pm0.83}$
0.6421	0.0017	$11.98^{\pm1.45}_{\pm0.94}$
0.6455	0.0017	$10.59^{\pm1.39}_{\pm0.83}$
0.649	0.0017	$7.70^{\pm1.21}_{\pm0.60}$
0.6525	0.0018	$7.39^{\pm1.20}_{\pm0.58}$
0.656	0.0018	$11.83^{\pm1.46}_{\pm0.93}$
0.6596	0.0018	$10.24^{\pm1.35}_{\pm0.80}$
0.6632	0.0018	$9.23^{\pm1.28}_{\pm0.72}$
0.6668	0.0018	$7.77^{\pm1.23}_{\pm0.61}$
0.6705	0.0018	$7.53^{\pm1.21}_{\pm0.59}$
0.6741	0.0018	$6.85^{\pm1.14}_{\pm0.54}$
0.6779	0.0019	$8.32^{\pm1.22}_{\pm0.65}$
0.6816	0.0019	$8.11^{\pm1.19}_{\pm0.63}$
0.6854	0.0019	$7.76^{\pm1.16}_{\pm0.61}$
0.6892	0.0019	$14.06^{\pm1.49}_{\pm1.10}$

TABLE VI. (*Continued.*)

E_n (MeV)	ΔE_n (MeV)	$\sigma^{\pm\text{stat}}_{\pm\text{sys}}$ (mb)
0.693	0.0019	$18.03^{\pm1.65}_{\pm1.41}$
0.6969	0.0019	$19.36^{\pm1.66}_{\pm1.51}$
0.7008	0.002	$22.19^{\pm3.44}_{\pm1.73}$
30.7047	0.002	$28.41^{\pm3.88}_{\pm2.22}$
0.7087	0.002	$33.42^{\pm4.28}_{\pm2.61}$
0.7127	0.002	$30.60^{\pm4.11}_{\pm2.38}$
0.7167	0.002	$27.54^{\pm3.94}_{\pm2.15}$
0.7208	0.002	$26.77^{\pm3.91}_{\pm2.08}$
0.7249	0.0021	$28.16^{\pm3.97}_{\pm2.19}$
0.729	0.0021	$24.88^{\pm3.74}_{\pm1.94}$
0.7332	0.0021	$24.99^{\pm3.87}_{\pm1.94}$
0.7374	0.0021	$21.99^{\pm3.49}_{\pm1.71}$
0.7416	0.0021	$23.61^{\pm3.63}_{\pm1.84}$
0.7459	0.0022	$29.81^{\pm3.90}_{\pm2.32}$
0.7502	0.0022	$36.58^{\pm4.27}_{\pm2.84}$
0.7546	0.0022	$39.02^{\pm4.44}_{\pm3.03}$
0.759	0.0022	$40.81^{\pm4.43}_{\pm3.17}$
0.7634	0.0022	$32.45^{\pm3.90}_{\pm2.52}$
0.7679	0.0022	$30.80^{\pm3.75}_{\pm2.39}$
0.7724	0.0023	$24.61^{\pm3.36}_{\pm1.91}$
0.7769	0.0023	$20.17^{\pm3.02}_{\pm1.56}$
0.7815	0.0023	$15.26^{\pm2.63}_{\pm1.18}$
0.7862	0.0023	$16.04^{\pm2.65}_{\pm1.24}$
0.7908	0.0023	$16.45^{\pm2.61}_{\pm1.27}$
0.7956	0.0024	$19.10^{\pm2.77}_{\pm1.48}$
0.8003	0.0024	$22.03^{\pm2.98}_{\pm1.70}$
0.8051	0.0024	$26.67^{\pm3.20}_{\pm2.06}$
0.81	0.0024	$29.01^{\pm3.39}_{\pm2.24}$
0.8149	0.0025	$33.42^{\pm3.62}_{\pm2.58}$
0.8198	0.0025	$44.62^{\pm4.27}_{\pm3.44}$
0.8248	0.0025	$50.61^{\pm4.64}_{\pm3.90}$
0.8298	0.0025	$53.27^{\pm4.94}_{\pm4.11}$
0.8349	0.0025	$45.75^{\pm4.39}_{\pm3.52}$
0.84	0.0026	$38.67^{\pm4.03}_{\pm2.98}$
0.8451	0.0026	$27.87^{\pm3.35}_{\pm2.15}$
0.8503	0.0026	$20.55^{\pm2.86}_{\pm1.58}$
0.8556	0.0026	$18.29^{\pm2.71}_{\pm1.41}$
0.8609	0.0027	$19.62^{\pm2.82}_{\pm1.51}$
0.8663	0.0027	$21.22^{\pm2.88}_{\pm1.63}$
0.8717	0.0027	$27.82^{\pm3.31}_{\pm2.14}$
0.8771	0.0027	$30.55^{\pm3.44}_{\pm2.35}$
0.8826	0.0028	$29.38^{\pm3.34}_{\pm2.25}$
0.8882	0.0028	$30.07^{\pm3.41}_{\pm2.31}$
0.8938	0.0028	$29.27^{\pm3.39}_{\pm2.24}$
0.8995	0.0028	$30.21^{\pm3.44}_{\pm2.31}$
0.9052	0.0029	$27.18^{\pm3.25}_{\pm2.08}$

TABLE VI. (*Continued.*)

E_n (MeV)	ΔE_n (MeV)	$\sigma^{\pm\text{stat}}_{\pm\text{sys}}$ (mb)
0.911	0.0029	$22.23^{\pm2.87}_{\pm1.70}$
0.9168	0.0029	$20.21^{\pm2.75}_{\pm1.55}$
0.9227	0.003	$16.24^{\pm2.42}_{\pm1.24}$
0.9287	0.003	$13.02^{\pm2.15}_{\pm0.99}$
0.9347	0.003	$13.45^{\pm2.16}_{\pm1.03}$
0.9407	0.003	$14.96^{\pm2.27}_{\pm1.14}$
0.9468	0.0031	$20.97^{\pm2.65}_{\pm1.60}$
0.953	0.0031	$23.25^{\pm2.79}_{\pm1.77}$
0.9593	0.0031	$34.53^{\pm3.55}_{\pm2.63}$
0.9656	0.0032	$41.73^{\pm3.97}_{\pm3.18}$
0.9719	0.0032	$58.64^{\pm5.11}_{\pm4.46}$
0.9784	0.0032	$57.73^{\pm4.93}_{\pm4.39}$
0.9849	0.0033	$63.60^{\pm5.30}_{\pm4.84}$
0.9914	0.0033	$66.33^{\pm5.43}_{\pm5.04}$
0.998	0.0033	$67.84^{\pm5.58}_{\pm5.15}$
1.0047	0.0034	$59.35^{\pm5.06}_{\pm4.50}$
1.0115	0.0034	$43.95^{\pm4.12}_{\pm3.33}$
1.0183	0.0034	$40.49^{\pm3.96}_{\pm3.07}$
1.0252	0.0035	$38.85^{\pm3.84}_{\pm2.94}$
1.0322	0.0035	$37.45^{\pm3.77}_{\pm2.84}$
1.0392	0.0035	$38.84^{\pm3.80}_{\pm2.94}$
1.0463	0.0036	$42.81^{\pm4.07}_{\pm3.24}$
1.0535	0.0036	$40.88^{\pm3.92}_{\pm3.09}$
1.0608	0.0036	$33.10^{\pm3.45}_{\pm2.50}$
1.0681	0.0037	$30.37^{\pm3.23}_{\pm2.29}$
1.0755	0.0037	$31.03^{\pm3.24}_{\pm2.34}$
1.083	0.0038	$36.99^{\pm3.63}_{\pm2.79}$
1.0905	0.0038	$41.63^{\pm3.87}_{\pm3.14}$
1.0982	0.0038	$42.64^{\pm3.91}_{\pm3.21}$
1.1059	0.0039	$48.44^{\pm4.28}_{\pm3.65}$
1.1137	0.0039	$50.39^{\pm4.40}_{\pm3.79}$
1.1216	0.004	$54.42^{\pm4.59}_{\pm4.09}$
1.1296	0.004	$54.87^{\pm4.57}_{\pm4.12}$
1.1377	0.0041	$49.86^{\pm4.27}_{\pm3.74}$
1.1458	0.0041	$48.97^{\pm4.24}_{\pm3.67}$
1.154	0.0041	$39.08^{\pm3.63}_{\pm2.93}$
1.1623	0.0042	$41.80^{\pm3.79}_{\pm3.13}$
1.1708	0.0042	$41.04^{\pm3.71}_{\pm3.07}$
1.1793	0.0043	$48.79^{\pm4.19}_{\pm3.65}$
1.1879	0.0043	$55.85^{\pm4.57}_{\pm4.18}$
1.1966	0.0044	$66.58^{\pm5.21}_{\pm4.98}$
1.2053	0.0044	$61.39^{\pm4.92}_{\pm4.58}$
1.2142	0.0045	$54.88^{\pm4.53}_{\pm4.10}$
1.2232	0.0045	$49.62^{\pm4.23}_{\pm3.70}$
1.2323	0.0046	$42.33^{\pm3.84}_{\pm3.16}$
1.2415	0.0046	$35.22^{\pm3.36}_{\pm2.62}$

TABLE VI. (*Continued.*)

E_n (MeV)	ΔE_n (MeV)	$\sigma^{\pm\text{stat}}_{\pm\text{sys}}$ (mb)
1.2508	0.0047	$31.43^{\pm3.14}_{\pm2.34}$
1.2602	0.0047	$27.80^{\pm2.93}_{\pm2.07}$
1.2697	0.0048	$32.42^{\pm3.23}_{\pm2.41}$
1.2793	0.0048	$30.70^{\pm3.05}_{\pm2.28}$
1.289	0.0049	$29.18^{\pm3.00}_{\pm2.17}$
1.2988	0.0049	$30.31^{\pm3.05}_{\pm2.25}$
1.3088	0.005	$33.52^{\pm3.23}_{\pm2.48}$
1.3188	0.0051	$33.22^{\pm3.23}_{\pm2.46}$
1.329	0.0051	$39.96^{\pm3.57}_{\pm2.96}$
1.3393	0.0052	$52.15^{\pm4.30}_{\pm3.86}$
1.3497	0.0052	$62.41^{\pm4.84}_{\pm4.61}$
1.3602	0.0053	$70.40^{\pm5.31}_{\pm5.20}$
1.3709	0.0054	$68.83^{\pm5.20}_{\pm5.08}$
1.3817	0.0054	$55.81^{\pm4.44}_{\pm4.12}$
1.3926	0.0055	$46.98^{\pm3.94}_{\pm3.46}$
1.4036	0.0056	$38.68^{\pm3.44}_{\pm2.85}$
1.4148	0.0056	$35.05^{\pm3.22}_{\pm2.58}$
1.4261	0.0057	$31.60^{\pm3.01}_{\pm2.32}$
1.4376	0.0058	$33.79^{\pm3.12}_{\pm2.48}$
1.4491	0.0058	$37.34^{\pm3.34}_{\pm2.74}$
1.4608	0.0059	$33.61^{\pm3.12}_{\pm2.47}$
1.4727	0.006	$33.71^{\pm3.12}_{\pm2.47}$
1.4847	0.006	$36.67^{\pm3.31}_{\pm2.69}$
1.4969	0.0061	$44.17^{\pm3.76}_{\pm3.23}$
1.5092	0.0062	$53.10^{\pm4.29}_{\pm3.88}$
1.5216	0.0063	$71.07^{\pm5.31}_{\pm5.19}$
1.5343	0.0063	$88.14^{\pm6.24}_{\pm6.44}$
1.547	0.0064	$96.72^{\pm6.70}_{\pm7.06}$
1.56	0.0065	$93.71^{\pm6.56}_{\pm6.83}$
1.5731	0.0066	$84.21^{\pm6.02}_{\pm6.14}$
1.5863	0.0067	$76.06^{\pm5.55}_{\pm5.54}$
1.5998	0.0068	$82.49^{\pm5.91}_{\pm6.00}$
1.6134	0.0068	$88.57^{\pm6.24}_{\pm6.44}$
1.6271	0.0069	$80.07^{\pm5.77}_{\pm5.82}$
1.6411	0.007	$76.41^{\pm5.56}_{\pm5.55}$
1.6552	0.0071	$74.29^{\pm5.44}_{\pm5.39}$
1.6695	0.0072	$67.89^{\pm5.09}_{\pm4.92}$
1.6841	0.0073	$58.97^{\pm4.58}_{\pm4.27}$
1.6987	0.0074	$57.31^{\pm4.48}_{\pm4.15}$
1.7136	0.0075	$64.37^{\pm4.85}_{\pm4.65}$
1.7287	0.0076	$62.08^{\pm4.72}_{\pm4.49}$
1.744	0.0077	$61.47^{\pm4.67}_{\pm4.44}$
1.7595	0.0078	$70.24^{\pm5.16}_{\pm5.07}$
1.7752	0.0079	$79.64^{\pm5.66}_{\pm5.74}$
1.7911	0.008	$85.65^{\pm5.98}_{\pm6.17}$
1.8072	0.0081	$100.47^{\pm6.77}_{\pm7.23}$

TABLE VI. (*Continued.*)

E_n (MeV)	ΔE_n (MeV)	$\sigma^{\pm\text{stat}}_{\pm\text{sys}}$ (mb)
1.8236	0.0082	$112.01^{\pm7.38}_{\pm8.06}$
1.8401	0.0083	$106.12^{\pm7.06}_{\pm7.63}$
1.8569	0.0085	$90.71^{\pm6.23}_{\pm6.51}$
1.8739	0.0086	$84.87^{\pm5.91}_{\pm6.09}$
1.8912	0.0087	$77.95^{\pm5.54}_{\pm5.59}$
1.9087	0.0088	$68.64^{\pm5.04}_{\pm4.92}$
1.9264	0.0089	$70.27^{\pm5.13}_{\pm5.03}$
1.9444	0.0091	$67.72^{\pm5.00}_{\pm4.85}$
1.9627	0.0092	$88.33^{\pm6.13}_{\pm6.32}$
1.9812	0.0093	$101.00^{\pm6.82}_{\pm7.22}$
1.9999	0.0094	$96.08^{\pm6.54}_{\pm6.86}$
2.019	0.0096	$79.79^{\pm5.68}_{\pm5.64}$
2.0383	0.0097	$59.76^{\pm4.59}_{\pm4.23}$
2.0579	0.0099	$58.39^{\pm4.51}_{\pm4.13}$
2.0777	0.01	$74.00^{\pm5.36}_{\pm5.23}$
2.0979	0.0102	$88.64^{\pm6.14}_{\pm6.27}$
2.1183	0.0103	$102.90^{\pm6.88}_{\pm7.28}$
2.1391	0.0105	$110.26^{\pm7.27}_{\pm7.80}$
2.1601	0.0106	$97.17^{\pm6.59}_{\pm6.87}$
2.1815	0.0108	$72.24^{\pm5.30}_{\pm5.11}$
2.2032	0.0109	$65.31^{\pm4.94}_{\pm4.62}$
2.2252	0.0111	$57.18^{\pm4.49}_{\pm4.04}$
2.2476	0.0113	$59.88^{\pm4.62}_{\pm4.23}$
2.2703	0.0114	$69.76^{\pm5.14}_{\pm4.93}$
2.2933	0.0116	$79.61^{\pm5.67}_{\pm5.63}$
2.3167	0.0118	$75.81^{\pm5.46}_{\pm5.36}$
2.3404	0.012	$72.06^{\pm5.28}_{\pm5.10}$
2.3646	0.0122	$70.16^{\pm5.20}_{\pm4.96}$
2.3891	0.0123	$74.04^{\pm5.43}_{\pm5.24}$
2.4139	0.0125	$85.11^{\pm6.04}_{\pm6.02}$
2.4392	0.0127	$93.46^{\pm6.50}_{\pm6.61}$
2.4649	0.0129	$90.13^{\pm6.32}_{\pm6.37}$
2.4909	0.0131	$84.03^{\pm6.02}_{\pm5.94}$
2.5174	0.0134	$87.92^{\pm6.21}_{\pm6.22}$
2.5443	0.0136	$99.23^{\pm6.79}_{\pm7.02}$
2.5717	0.0138	$120.09^{\pm7.85}_{\pm8.49}$
2.5995	0.014	$136.07^{\pm8.68}_{\pm9.62}$
2.6277	0.0142	$138.43^{\pm8.79}_{\pm9.79}$
2.6564	0.0145	$134.88^{\pm8.60}_{\pm9.54}$
2.6856	0.0147	$128.00^{\pm8.25}_{\pm9.05}$
2.7153	0.015	$119.25^{\pm7.78}_{\pm8.43}$
2.7454	0.0152	$113.16^{\pm7.49}_{\pm8.00}$
2.7761	0.0155	$117.58^{\pm7.72}_{\pm8.31}$
2.8073	0.0157	$120.34^{\pm7.88}_{\pm8.51}$
2.839	0.016	$126.55^{\pm8.20}_{\pm8.95}$
2.8713	0.0163	$139.94^{\pm8.87}_{\pm9.90}$
2.9041	0.0165	$143.13^{\pm9.03}_{\pm10.12}$
2.9375	0.0168	$137.29^{\pm8.75}_{\pm9.71}$

TABLE VI. (*Continued.*)

E_n (MeV)	ΔE_n (MeV)	$\sigma^{\pm\text{stat}}_{\pm\text{sys}}$ (mb)
2.9714	0.0171	$135.98^{\pm8.68}_{\pm9.62}$
3.006	0.0174	$123.20^{\pm8.02}_{\pm8.71}$
3.0411	0.0177	$143.04^{\pm9.03}_{\pm10.12}$
3.0769	0.018	$164.04^{\pm10.10}_{\pm11.60}$
3.1133	0.0184	$147.00^{\pm9.24}_{\pm10.39}$
3.1504	0.0187	$133.40^{\pm8.57}_{\pm9.43}$
3.1881	0.019	$133.30^{\pm8.60}_{\pm9.43}$
3.2265	0.0194	$130.09^{\pm8.46}_{\pm9.20}$
3.2656	0.0197	$132.39^{\pm8.60}_{\pm9.36}$
3.3055	0.0201	$153.75^{\pm9.69}_{\pm10.87}$
3.346	0.0205	$159.10^{\pm9.96}_{\pm11.25}$
3.3874	0.0209	$156.12^{\pm9.84}_{\pm11.04}$
3.4295	0.0212	$163.00^{\pm10.20}_{\pm11.53}$
3.4723	0.0216	$171.41^{\pm10.62}_{\pm12.12}$
3.516	0.0221	$169.28^{\pm10.52}_{\pm11.97}$
3.5606	0.0225	$177.61^{\pm10.95}_{\pm12.56}$
3.6059	0.0229	$159.13^{\pm10.05}_{\pm11.25}$
3.6522	0.0233	$152.50^{\pm9.72}_{\pm10.78}$
3.6993	0.0238	$145.01^{\pm9.37}_{\pm10.25}$
3.7474	0.0243	$142.89^{\pm9.35}_{\pm10.10}$
3.812	0.062	$150.34^{\pm3.25}_{\pm10.63}$
3.938	0.062	$152.13^{\pm3.39}_{\pm10.76}$
4.062	0.062	$171.79^{\pm3.29}_{\pm12.15}$
4.188	0.062	$170.99^{\pm3.35}_{\pm12.09}$
4.312	0.062	$180.16^{\pm3.50}_{\pm12.74}$
4.438	0.062	$194.34^{\pm3.71}_{\pm13.74}$
4.562	0.062	$197.07^{\pm3.82}_{\pm13.94}$
4.688	0.062	$206.21^{\pm3.97}_{\pm14.58}$
4.812	0.062	$192.38^{\pm3.89}_{\pm13.61}$
4.938	0.062	$197.77^{\pm4.03}_{\pm13.99}$
5.062	0.062	$212.66^{\pm4.27}_{\pm15.05}$
5.188	0.062	$202.15^{\pm4.27}_{\pm14.31}$
5.312	0.062	$209.22^{\pm4.43}_{\pm14.85}$
5.438	0.062	$205.44^{\pm4.47}_{\pm14.62}$
5.562	0.062	$217.55^{\pm4.70}_{\pm15.49}$
5.688	0.062	$220.80^{\pm4.82}_{\pm15.81}$
5.812	0.062	$194.91^{\pm4.71}_{\pm14.53}$
5.938	0.062	$190.93^{\pm4.76}_{\pm15.06}$
6.062	0.062	$200.67^{\pm4.86}_{\pm15.14}$
6.188	0.062	$194.25^{\pm4.95}_{\pm15.62}$
6.312	0.062	$184.33^{\pm5.01}_{\pm15.81}$
6.438	0.062	$190.13^{\pm5.08}_{\pm15.45}$
6.562	0.062	$195.67^{\pm4.98}_{\pm15.09}$
6.688	0.062	$199.96^{\pm5.07}_{\pm15.33}$
6.812	0.062	$186.38^{\pm6.63}_{\pm14.68}$
6.938	0.062	$195.10^{\pm5.06}_{\pm14.92}$
7.062	0.062	$190.92^{\pm5.22}_{\pm15.43}$

TABLE VII. Measured cross sections for $(n, \alpha_{\text{total}})$ at a flight path length of 15.2 m.

E_n (MeV)	$\sigma^{\pm\text{stat}}_{\pm\text{sys}}$ (mb)
2.8 ± 0.05	$19.47^{\pm 5.92}_{\pm 1.88}$
2.9 ± 0.05	$16.87^{\pm 4.02}_{\pm 1.63}$
3 ± 0.05	$27.12^{\pm 6.01}_{\pm 2.61}$
3.1 ± 0.05	$27.65^{\pm 5.79}_{\pm 2.66}$
3.2 ± 0.05	$42.9^{\pm 8.27}_{\pm 4.13}$
3.3 ± 0.05	$57.38^{\pm 8.23}_{\pm 5.53}$
3.4 ± 0.05	$60.57^{\pm 6.90}_{\pm 5.84}$
3.5 ± 0.05	$58.37^{\pm 7.21}_{\pm 5.62}$
3.6 ± 0.05	$62.55^{\pm 6.62}_{\pm 6.03}$
3.7 ± 0.1	$71.26^{\pm 7.42}_{\pm 6.87}$
3.9 ± 0.1	$92.41^{\pm 3.39}_{\pm 5.11}$
4.1 ± 0.1	$115.74^{\pm 3.87}_{\pm 6.40}$
4.3 ± 0.1	$130.38^{\pm 4.09}_{\pm 7.19}$
4.5 ± 0.1	$131.82^{\pm 4.22}_{\pm 7.28}$
4.7 ± 0.1	$145.33^{\pm 4.54}_{\pm 8.01}$
4.9 ± 0.1	$150.87^{\pm 4.82}_{\pm 8.36}$
5.1 ± 0.1	$157.83^{\pm 5.03}_{\pm 8.71}$
5.3 ± 0.1	$170.4^{\pm 5.30}_{\pm 9.36}$
5.5 ± 0.1	$186.15^{\pm 5.70}_{\pm 10.24}$
5.75 ± 0.15	$178.1^{\pm 4.69}_{\pm 9.80}$
6.05 ± 0.15	$190.94^{\pm 5.12}_{\pm 10.50}$
6.35 ± 0.15	$173.65^{\pm 5.02}_{\pm 9.59}$
6.65 ± 0.15	$192.09^{\pm 5.60}_{\pm 10.57}$
6.95 ± 0.15	$177.53^{\pm 5.59}_{\pm 9.79}$
7.25 ± 0.15	$183.04^{\pm 6.02}_{\pm 10.06}$
7.55 ± 0.15	$187.15^{\pm 6.81}_{\pm 10.35}$
7.85 ± 0.15	$187.39^{\pm 6.96}_{\pm 10.35}$
8.25 ± 0.25	$192.01^{\pm 5.74}_{\pm 10.57}$
8.75 ± 0.25	$177.32^{\pm 6.02}_{\pm 9.80}$
9.25 ± 0.25	$175.79^{\pm 6.34}_{\pm 9.73}$
9.75 ± 0.25	$181.6^{\pm 6.87}_{\pm 10.03}$
10.25 ± 0.25	$173.56^{\pm 8.13}_{\pm 11.62}$
10.75 ± 0.25	$182.65^{\pm 8.86}_{\pm 12.23}$
11.25 ± 0.25	$169.99^{\pm 9.41}_{\pm 11.39}$
11.75 ± 0.25	$198.17^{\pm 9.92}_{\pm 13.27}$
12.25 ± 0.25	$175.1^{\pm 10.19}_{\pm 11.73}$

TABLE VIII. Measured cross sections for $(n, \alpha_{\text{total}})$ at a flight path length of 8.2 m.

E_n (MeV)	$\sigma^{\pm\text{stat}}_{\pm\text{sys}}$ (mb)
2.025 ± 0.125	$1.11^{\pm 0.09}_{\pm 0.11}$
2.275 ± 0.125	$2.61^{\pm 0.14}_{\pm 0.26}$
2.525 ± 0.125	$7.23^{\pm 0.24}_{\pm 0.72}$
2.775 ± 0.125	$16.51^{\pm 0.39}_{\pm 1.63}$
3.025 ± 0.125	$27.45^{\pm 0.52}_{\pm 2.72}$
3.275 ± 0.125	$48.41^{\pm 0.72}_{\pm 4.79}$
3.525 ± 0.125	$62.72^{\pm 0.93}_{\pm 6.21}$
3.775 ± 0.125	$83.85^{\pm 1.20}_{\pm 8.30}$
4.025 ± 0.125	$112.21^{\pm 1.50}_{\pm 11.11}$
4.275 ± 0.125	$138.18^{\pm 1.79}_{\pm 13.68}$
4.525 ± 0.125	$157.66^{\pm 2.06}_{\pm 15.61}$
4.775 ± 0.125	$169.73^{\pm 2.28}_{\pm 16.80}$
5.025 ± 0.125	$187.34^{\pm 2.56}_{\pm 18.55}$
5.275 ± 0.125	$184.41^{\pm 2.71}_{\pm 18.26}$
5.525 ± 0.125	$200.10^{\pm 2.96}_{\pm 19.81}$
5.775 ± 0.125	$204.80^{\pm 3.11}_{\pm 20.28}$
6.025 ± 0.125	$197.50^{\pm 3.17}_{\pm 19.56}$
6.275 ± 0.125	$201.50^{\pm 3.31}_{\pm 19.96}$
6.525 ± 0.125	$190.50^{\pm 3.33}_{\pm 18.88}$
6.775 ± 0.125	$191.99^{\pm 3.45}_{\pm 19.05}$
7.025 ± 0.125	$188.60^{\pm 3.54}_{\pm 18.83}$
7.275 ± 0.125	$194.98^{\pm 3.74}_{\pm 19.66}$
7.525 ± 0.125	$189.03^{\pm 3.84}_{\pm 19.50}$
7.775 ± 0.125	$198.92^{\pm 4.10}_{\pm 21.05}$
8.025 ± 0.125	$195.90^{\pm 4.24}_{\pm 21.72}$
8.275 ± 0.125	$186.56^{\pm 4.25}_{\pm 21.25}$
8.525 ± 0.125	$198.37^{\pm 4.52}_{\pm 23.32}$
8.775 ± 0.125	$206.16^{\pm 4.69}_{\pm 24.61}$
9.025 ± 0.125	$204.04^{\pm 4.88}_{\pm 25.39}$
9.275 ± 0.125	$205.62^{\pm 5.06}_{\pm 26.54}$
9.525 ± 0.125	$199.83^{\pm 5.24}_{\pm 27.33}$
9.775 ± 0.125	$205.19^{\pm 5.44}_{\pm 28.66}$
10.025 ± 0.125	$194.55^{\pm 5.50}_{\pm 29.03}$

[1] S. A. Kuvin, H. Y. Lee, T. Kawano, B. DiGiovine, A. Georgiadou, C. Vermeulen, M. White, L. Zavorka, and H. I. Kim, Phys. Rev. C **102**, 024623 (2020).
[2] R. L. Macklin, Phys. Rev. C **29**, 1996 (1984).
[3] P. E. Koehler, Phys. Rev. C **44**, 1675 (1991).
[4] S. Druyts, C. Wagemans, and P. Geltenbort, Nucl. Phys. A **573**, 291 (1994).
[5] L. De Smet, C. Wagemans, G. Goeminne, J. Heyse, and J. Van Gils, Phys. Rev. C **75**, 034617 (2007).
[6] R. O. Sayer, K. H. Guber, L. C. Leal, N. M. Larson, and T. Rauscher, Phys. Rev. C **73**, 044603 (2006).
[7] D. A. Brown, M. B. Chadwick, R. Capote, A. C. Kahler, A. Trkov, M. W. Herman, A. A. Sonzogni, Y. Danon, A. D. Carlson, M. Dunn, D. L. Smith, G. M. Hale, G. Arbanas, R. Arcilla, C. R. Bates, B. Beck, B. Becker, F. Brown, R. J. Casperson, J. Conlin *et al.*, Nucl. Data Sheets **148**, 1 (2018).
[8] O. Iwamoto, N. Iwamoto, S. Kunieda, F. Minato, S. Nakayama, Y. Abe, K. Tsubakihara, S. Okumura, C. Ishizuka, T. Yoshida, S. Chiba, N. Otuka, J.-C. Sublet, H. Iwamoto, K. Yamamoto, Y. Nagaya, K. Tada, C. Konno, N. Matsuda, K. Yokoyama *et al.*, J. Nuc. Sci. & Tech. **60**, 1 (2023).
[9] F. Metzger, P. Huber, and F. Adler, Helv. Phys. Act. **20**, 236 (1947).
[10] H. Adler, P. Huber, and W. Haelg, Helv. Phys. Act. **26**, 349 (1953).
[11] D. B. Nichols, B. D. Kern, and M. T. McEllistrem, Phys. Rev. **151**, 879 (1966).
[12] S. Cierjacks, P. Forti, D. Kopsch, L. Kropp, J. Nebe, and H. Unseld, Kernforschungszentrum Karlsruhe Rep. **SUPP.2**, 1000 (1969).
[13] U. Fasoli, P. P. Sambo, D. Toniolo, and G. Zago, Report from Euratom-countries + Euratom to EANDC **89** (1968).
[14] D. G. Foster and D. W. Glasgow, Phys. Rev. C **3**, 576 (1971).
[15] U. N. Singh, H. I. Liou, G. Hacken, M. Slagowitz, F. Rahn, J. Rainwater, W. Makofske, and J. B. Garg, Phys. Rev. C **10**, 2138 (1974).
[16] D. E. Holcomb, G. F. Flanagan, B. W. Patton, J. C. Gehin, R. L. Howard, and T. J. Harrison, ORNL/TM-2011/105 (2011).
[17] Y. Tahara, H. Hirano, S. Chiba, H. Mochizuki, and T. Katabuchi, J. Nuc. Sci. & Tech. **61**, 277 (2024).
[18] T. Taylor, A. Ballard, A. Fernandez, Y. Cao, W. S. Yang, B. Feng, and T. Hua, *Proceedings from the 41st Annual Conference of the Canadian Nuclear Society and 46th Annual CNS/CNA Student Conference, Saint John, NB, June 5–June 8, 2022*, https://www.moltexenergy.com/wp-content/uploads/CNS-2022-Paper-Sensitivity-to-chlorine-nuclear-data.pdf.
[19] A. T. Cisneros and T. Taylor, https://www.oecd-nea.org/dbdata/hprl/hprlview.pl?ID=540.
[20] M. B. Smith, T. Achtzehn, H. R. Andrews, E. T. H. Clifford, P. Forget, J. Glodo, R. Hawrami, H. Ing, P. O'Dougherty, K. S. Shah, U. Shirwadkar, L. Soundara-Pandian, and J. Tower, Nucl. Instrum. Meth. Phys. Res. A **784**, 162 (2015).
[21] J. C. Batchelder, S.-A. Chong, J. Morrell, M. A. Unzueta, P. Adams, J. D. Bauer, T. Bailey, T. A. Becker, L. A. Bernstein, M. Fratoni, A. M. Hurst, J. James, A. M. Lewis, E. F. Matthews, M. Negus, D. Rutte, K. Song, K. Van Bibber, M. Wallace, and C. S. Waltz, Phys. Rev. C **99**, 044612 (2019).
[22] E. Sansarbayar, Y. M. Gledenov, I. Chuprakov, G. Khuukhenkhuu, G. S. Ahmadov, L. Krupa, G. Zhang, H. Jiang, Z. Cui, Y. Hu, J. Liu, N. Battsooj, I. Wilhelm, M. Solar, R. Sykora, and Z. Kohout, Phys. Rev. C **104**, 044620 (2021).
[23] J. N. Warren, Master's Thesis, Ohio University, 2021.
[24] G. Palmiotti, J. C. Gehin, and T. Cisneros, OSTI No. 1891907, Report No. INL/CON-21-64838-Rev000, Idaho National Lab. (INL), Idaho Falls, ID, United States, 2021, https://www.osti.gov/biblio/1891907.
[25] S. A. Kuvin, H. Y. Lee, B. DiGiovine, C. Eiroa-Lledo, A. Georgiadou, M. Herman, T. Kawano, V. Mocko, S. Mosby, C. Vermeulen, D. Votaw, M. White, L. Zavorka, G. Perdikakis, P. Tsintari, and H. I. Kim, Phys. Rev. C **105**, 044608 (2022).
[26] A. D. Carlson, V. G. Pronyaev, R. Capote, G. M. Hale, Z.-P. Chen, I. Duran, F.-J. Hambsch, S. Kunieda, W. Mannhart, B. Marcinkevicius, R. O. Nelson, D. Neudecker, G. Noguere, M. Paris, S. P. Simakov, P. Schillebeeckx, D. L. Smith, X. Tao, A. Trkov, A. Wallner *et al.*, Nucl. Data Sheets **148**, 143 (2018).
[27] R. Song, X. Yan, J. Han, X. Luo, F. Ren, Y. Zhang, Z. Han, C. Wen, X. Zhang, L. Chen, W. Lin, G. Qu, X. Liu, Q. Leng, J. Zhu, S. Qian, and Z. Wang, IEEE Trans. Nucl. Sci. **70**, 2148 (2023).
[28] T. Nagel, Ph.D. thesis, University of California, Berkeley, 2024.
[29] Y. M. Verzilov, F. Maekawa, Y. Oyama, and Y. Ikeda, Fus. Eng. & Des. **37**, 95 (1997).
[30] T. Kawano, Eur. Phys. J. A **57**, 16 (2021).
[31] S. Kunieda, S. Chiba, K. Shibata, A. Ichihara, and E. S. Sukhovitski, J. Nucl. Sci. Technol. **44**, 838 (2007).
[32] P. Möller, J. R. Nix, W. D. Myer, and W. J. Swiatecki, At. Data Nucl. Data Tables **59**, 185 (1995).
[33] L. Y. Kazakova, V. E. Kolesov, V. I. Popov, O. A. Salnikov, V. M. Sluchevskaja, and V. I. Trikova, Euro.-Am. Nucl. Dat. Comm. **2**, 200 (1965).
[34] G. Bonazzola, E. Chiavassa, and T. Bressani, Nuov. Cim. B **45**, 60 (1966).
[35] B. Leshchenko, G. Nurabaeva, and Y. Onishchuk, Vestnik Kiev State Univ. **28**, 74 (1987).
[36] R. E. Kalman, J. Basic Eng. D **82**, 35 (1960).
[37] P. Möller, A. J. Sierk, T. Ichikawa, and H. Sagawa, At. Data Nucl. Data Tables **109-110**, 1 (2016).
[38] A. Gilbert and A. G. W. Cameron, Can. J. Phys. **43**, 1446 (1965).
[39] T. Kawano, S. Chiba, and H. Koura, J. Nucl. Sci. Technol. **43**, 1 (2006).
[40] T. Kawano and F. H. Fröhner, Nucl. Sci. Eng. **127**, 130 (1997).
[41] D. V. Aleksandrov, L. I. Klochkova, and B. S. Kovrigin, Atomnaya Energiya **39**, 137 (1975).
[42] W. Nagel, Ph.D. thesis, University of Amsterdam, Amsterdam, 1966, http://www-nds.iaea.org/EXFOR/20198.006.
[43] W. Schantl, Ph.D. thesis, Inst. fuer Isotopenforschung und Kernphysik, Vienna, 1970, http://www-nds.iaea.org/EXFOR/21846.023.
[44] V. Avrigeanu, M. Avrigeanu, and C. Mănăilesc, Phys. Rev. C **90**, 044612 (2014).
[45] V. N. Levkovskii, J. Exp. & Theo. Phys. **18**, 213 (1964).
[46] R. C. Barrall, J. A. Holmes, and M. Silbergeld, Air Force Spec. Weap. Center Kirtland A.F.B. Repts., 68 (1969).
[47] E. B. Paul and R. L. Clarke, Can. J. Phys. **31**, 267 (1953).
[48] R. S. Scalan and R. W. Fink, Nucl. Phys. **9**, 334 (1958).
[49] L. McFadden and G. R. Satchler, Nucl. Phys. **84**, 177 (1966).
[50] R. Capote, M. Herman, P. Oblozinsky, P. G. Young, S. Goriely, T. Belgya, A. V. Ignatyuk, A. J. Koning, S. Hilaire, V. A. Plujko, M. Avrigeanu, O. Bersillon, M. B. Chadwick, T. Fukahori, Z. Ge, Y. Han, S. Kailas, J. Kopecky, V. M. Maslov, G. Reffo *et al.*, Nucl. Data Sheets **110**, 3107 (2009).

[51] C. Kalbach, Phys. Rev. C **33**, 818 (1986).
[52] J. Araminowicz and J. Dresler, Inst. Badan Jadr. (Nucl. Res.), Swierk + Warsaw, Repts. 14, 1973.
[53] M. Belgaid, M. Siad, and M. Allab, J. Radioanaly. & Nuc. Chem. **166**, 493 (1992).
[54] A. Fessler, A. J. M. Plompen, D. L. Smith, J. W. Meadows, and Y. Ikeda, Nucl. Sci. Eng. **134**, 171 (2000).
[55] M. Hyvönen-Dabek, M. Tarvainen, and P. Holmberg, J. Radioanal. Chem. **46**, 357 (1978).
[56] Y. Ikeda, C. Konno, K. Oishi, T. Nakamura, H. Miyade, K. Kawade, H. Yamamoto, and T. Katoh, JAERI Reports, 1312 (1988).
[57] N. I. Molla, R. U. Miah, S. Basunia, S. M. Hossain, and M. Rahman, Conf. on Nucl. Data for Sci. and Techn. **1**, 517 (1997).
[58] A. Pasquarelli, Nucl. Phys. A **93**, 218 (1967).
[59] R. Pepelnik, B. Anders, B. M. Bahal, and M. Farooq, Ges. Kernen.-Verwertung, Schiffbau and Schiffahrt (1986).
[60] C. V. Srinivasa Rao, N. Lakshmana Das, B. V. Thirumala Rao, and J. Rama Rao, 21st Nucl. Phys. and Solid State Phys. Symp. Bombay **2**, 113 (1978).
[61] J. P. Gupta, H. D. Bhardwaj, and R. Prasad, Pramana **24**, 637 (1985).
[62] K. J. Kelly, M. Devlin, J. M. O'Donnell, E. A. Bennett, M. Paris, and P. A. Copp, Phys. Rev. C **108**, 014603 (2023).
[63] C. D. Pruitt, R. J. Charity, L. G. Sobotka, J. M. Elson, D. E. M. Hoff, K. W. Brown, M. C. Atkinson, W. H. Dickhoff, H. Y. Lee, M. Devlin, N. Fotiades, and S. Mosby, Phys. Rev. C **102**, 034601 (2020).
[64] A. Stamatopoulos, P. Koehler, A. Couture, B. DiGiovine, G. Rusev, and J. Ullmann, Nucl. Instrum. Meth. Phys. Res. A **1025**, 166166 (2022).
[65] Y. Kasugai, H. Yamamoto, K. Kawade, and T. Iida, Ann. Nucl. Energy **25**, 23 (1998).
[66] P. N. Ngoc, S. Gueth, F. Deak, and A. Kiss, Ph.D. thesis, Eotvos Lorand University, Budapest, 1980, http://www-nds.iaea.org/EXFOR/30562.007.
[67] B. Mitra, Nucl. and Solid State Physics Symp., Kanpur, 367 (1967).
[68] S. C. Mathur and I. Morgan, Nucl. Phys. **75**, 561 (1966).
[69] R. Prasad, D. C. Sarkar, and C. S. Khurana, Nucl. Phys. **85**, 476 (1966).
[70] A. Gottardo, G. Andreetta, and R. Lombardi, Nucl. Instrum. Meth. Phys. Res. A **1041**, 167332 (2022).
[71] D. Rigamonti, G. Q. Zhong, G. Croci, L. Giacomelli, G. Gorini, Z. Hu, A. Muraro, M. Nocente, E. Perelli Cippo, M. Rebai, M. Tardocchi, F. Camera, C. Cattadori, R. J. Zhou, L. Q. Hu, L. Ge, Y. Zhang, and T. S. Fan, J. Instr. **14**, C09025 (2019).
[72] B. Pritychenko and S. F. Mughabghab, Nucl. Data Sheets **113**, 3120 (2012).
[73] R. H. Cyburt, A. M. Amthor, R. Ferguson, Z. Meisel, K. Smith, S. Warren, A. Heger, R. D. Hoffman, T. Rauscher, A. Sakharuk, H. Schatz, F. K. Thielemann, and M. Wiescher, Astrophys. J. Suppl. Ser. **189**, 240 (2010).
[74] G. Pfrepper, Isotopes Envir. Health Studies **13**, 15 (1977).
[75] V. Hayodom, W. Boonkong, S. Mahapanyawong, and C. Chaimonkon, Prog: Atomic Energy for Peace, Bangkok Reports (1969).
[76] M. A. Arribére, S. Guevara, A. Kestelman *et al.*, J. Radioanal Nucl. Chem. **241**, 25 (1999).
[77] W. Z. Tian and M. D. Glascock, International J. Rad. Appl. Instrum. A **39**, 181 (1988).
[78] T. D. Bohm and B. A. Lindley, Fus. Sci. & Tech. **79**, 995 (2023).
[79] T. Cisneros, M. Wargon, K. Hanselman, T. Kawano, S. A. Kuvin, and H. Y. Lee, *Proceedings of the International Conference on Physics of Reactors (PHYSOR 2024), San Francisco, CA, 2024* (American Nuclear Society, 2024), pp. 1549–1559, https://www.ans.org/pubs/proceedings/article-55624/.